

Accepted Manuscript

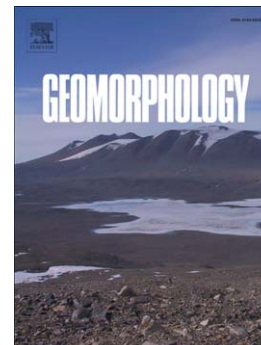
Cosmic ray exposure dating on the large landslide of Séchilienne (Western Alps): A synthesis to constrain the slope evolution

Stéphane Schwartz, Swann Zerathe, Denis Jongmans, Laurent Baillet, Julien Carcaillet, Laurence Audin, Thierry Dumont, Didier Bourlès, Régis Braucher, Vincent Lebrouc

PII: S0169-555X(16)30524-4
DOI: doi:[10.1016/j.geomorph.2016.11.014](https://doi.org/10.1016/j.geomorph.2016.11.014)
Reference: GEOMOR 5836

To appear in: *Geomorphology*

Received date: 27 June 2016
Accepted date: 16 November 2016



Please cite this article as: Schwartz, Stéphane, Zerathe, Swann, Jongmans, Denis, Baillet, Laurent, Carcaillet, Julien, Audin, Laurence, Dumont, Thierry, Bourlès, Didier, Braucher, Régis, Lebrouc, Vincent, Cosmic ray exposure dating on the large landslide of Séchilienne (Western Alps): A synthesis to constrain the slope evolution, *Geomorphology* (2016), doi:[10.1016/j.geomorph.2016.11.014](https://doi.org/10.1016/j.geomorph.2016.11.014)

This is a PDF file of an unedited manuscript that has been accepted for publication. As a service to our customers we are providing this early version of the manuscript. The manuscript will undergo copyediting, typesetting, and review of the resulting proof before it is published in its final form. Please note that during the production process errors may be discovered which could affect the content, and all legal disclaimers that apply to the journal pertain.

Cosmic ray exposure dating on the large landslide of Séchilienne (Western Alps): a synthesis to constrain the slope evolution.

Stéphane Schwartz^{1*}, Swann Zerathe¹, Denis Jongmans¹, Laurent Baillet¹, Julien Carcaillet¹, Laurence Audin¹, Thierry Dumont¹, Didier Bourlès², Régis Braucher², Vincent Lebrouc¹

1-Université Grenoble Alpes, CNRS, IRD, ISTERre, F-38000 Grenoble

2-CEREGE, Université Aix-Marseille-CNRS, France

*Corresponding author. Tel: 33 4 76 63 59 04; Fax: 33 4 76 51 40 58

E-mail address: stephane.schwartz@univ-grenoble-alpes.fr

Abstract

The $60 \times 10^6 \text{ m}^3$ Séchilienne landslide (Belledonne Massif, Western Alps) locates on the right bank of the East-West trending Romanche valley, shaped by glacial and alluvial processes during the Quaternary. Previous cosmic ray exposure (CRE) dating on the main scarp (Le Roux et al., 2009) revealed that the initiation of instability occurred several thousand years after ice down-wastage in the valley but the internal evolution of the landslide remained unknown. In this paper, we provide 63 additional ^{10}Be samples collected from the internal scarps and the main scarp, as well as on glacially polished rock surfaces. The aim is to constrain the global landslide kinematics and its possible relation to the glacier retreat. Results from glacially polished surfaces point out that complex shielding processes (relict moraines, soil deposits and seasonal snow cover) might have occurred after the glacial retreat. Despite age scattering resulting from these processes, our dataset evidence a glacial retreat achieved between 17.5 and 13 ka. Exposure ages obtained on gravitational scarps revealed that the landslide initiation occurred 8 to 6 ka ago. At this stage and until 2 ka the

gravitational kinematics was slow ($\sim 2 \text{ mm.yr}^{-1}$) and focused around on the main scarp, leading to a general slope subsidence. After 2 ka, the rates increased significantly ($\sim 8 \text{ mm.yr}^{-1}$) in association with the development of pervasive internal deformation of the landslide mass. This new slope evolution scenario of the Séchilienne area reflects progressive rock-slope weakening since 8 ka, associated to a continuous activity of a deep-seated failure surface.

Keywords: Western Alps, Séchilienne landslide, cosmic ray exposure dating, slope evolution.

1. Introduction

Alpine valley morphology has been strongly influenced by glaciations that have probably been the predominant erosional mechanism affecting glaciated mountain belts over the Quaternary (Montgomery, 2002 and references therein). The imprint of glacial erosion in the landscape is expressed by typical features such as U-shaped and overdeepened valleys, hanging valleys, stepped profiles, polished and striated surfaces and grooves, associated with the deposition of erosional products in moraines (Kelly et al., 2004; Anderson and Anderson, 2012). Numerous erosion models have been developed to explain how ice is able to shape the relief, both on longitudinal and transverse valley profiles (Harbor, 1992; Augustinus, 1995; McGregor et al., 2000; Anderson et al., 2006, Herman and Braun, 2008). In particular, Harbor (1992 and 1995) simulated the evolution of transverse valley profile during steady occupation by a glacier, showing that the valley propagates vertically as a U-shape form with lateral steepened rock-slopes. Numerous studies of longitudinal profiles of glaciated valleys have shown the presence of steps that usually coincide with coalescence of headwater valleys, tributary junctions or variations in rock resistance (McGregor et al., 2000; Anderson et al., 2006). It turned out that glacial erosion and the resulting landscape are strongly controlled by the bedrock hardness and strength, as well as by the fracturing (Dunforth et al. 2010, Krabbendam and Glasser, 2011; Salcher et al., 2014).

Deglaciation in the Alps left many slopes oversteepened, which have been subsequently affected by large rock-slope instabilities (Erismann and Abele, 2001). The cause usually cited for triggering rock-slope failure in deglaciated mountain areas is the lateral stress release resulting from ice melting (debutressing) (among others, Cruden and Hu, 1993; Blair, 1994; Evans and Clague, 1994; Holm et al., 2004; Cossart et al., 2008). However, the initiation of large-scale landslides in the Alps has also been associated with other factors like earthquakes, subsequent climatic changes, tectonic stresses, uplift rate and river and bedrock

erosion (e.g., Ballantyne, 2002; Seijmonsbergen et al., 2005; Cossart et al., 2008; Hormes et al., 2008; Le Roux et al., 2009; Sanchez et al., 2009, Zerathe et al., 2014). As all these factors are potentially active, identifying the major cause responsible for triggering rock-slope instability remains a strongly debated question (Korup, 2008; Zerathe et al., 2014) and the timing of events is a key issue to better understand the real mechanism(s) driving instabilities in a post-glacial period.

In the last decade, CRE (Cosmic Ray Exposure) dating has been increasingly and extensively used for assessing the timing of large rock-slope failures in the Alps (among others, Ivy-Ochs et al., 1998; Bigot-Cormier et al., 2005; Hippolyte et al., 2006; Hormes et al., 2008, Le Roux et al., 2009; Ivy-Ochs et al., 2009; Delunel et al., 2010a; Ostermann et al., 2012). The same technique was also applied to constrain the timing of the last deglaciation by dating late glacial moraine deposits and glacially polished bedrock surfaces (e.g. Darnault et al., 2012), allowing the chronology of both valley deglaciation and rock-slope instability to be established at specific sites (Bigot-Cormier et al., 2005; Cossart et al., 2008; Hormes et al., 2008; Ivy-Ochs et al., 2009; Prager et al., 2009, Le Roux et al. 2009; Martin et al., 2014). Major findings are that the last glacial retreat occurred simultaneously across the Alps (Darnault et al., 2012) and that some large landslides did not trigger during deglaciation but after a delay of several thousand years after the valley is ice-free (Le Roux et al., 2009; McColl, 2012). A recent synthesis of the failure-ages chronicles obtained for the large-scale landslides throughout the Alps (Zerathe et al., 2014) identified two main periods of landslide activity, from 11 to 8 ka (Pre-Boreal and Boreal periods) and from 5 to 3 ka (Subboreal period). The authors related the first activity period (11 to 8 ka) to two alpine-glacier recession phases at 10.9 ± 1.1 ka (end of the Younger Dryas period) and 8.4 ± 0.9 ka (beginning of the Holocene climatic optimum) (Darnault et al., 2012) and proposed the isostatic rebound following the glacial retreat as the main triggering factor. However, during

those two periods, the lower elevation valleys were totally deglaciated, as shown by Le Roux et al. (2009) and Martin et al. (2014), and have then been unaffected by the subsequent glacial retreats which occurred at higher elevations. Indeed, even for higher elevations, the documented cases (McColl, 2012) indicate that most large post-glacial failures have typically occurred some thousands of years after ice retreat (Hormes et al., 2008; Ivy-Ochs et al. 2009, Prager et al., 2009; Le Roux et al., 2009; Martin et al., 2014). Three main reasons have been generally evoked to explain this delay (McColl, 2012): the time lag between local slope stress-redistribution and the development of sheeting joints, the lag between regional glacio-isostatic rebound and a potential period of enhanced seismicity, and the effect of climatic factors such as warmer temperatures and increased rainfall which were more significant in the middle and early Holocene (Le Roux et al., 2009; Zerathe et al., 2014). Recently, Lebrouc et al. (2013) also proposed that the persistence of permafrost could have played a role in delaying instability initiation. Modeling the thermal response of the Séchilienne slope (Romanche valley, Western Alps) during the last 21,000 years, they suggested that the permafrost probably vanished around 10 to 11 ka, at least 3000 to 4000 years after the total ice down-wastage in the valley.

Most of the CRE studies on large landslides were focused on the dating of head scarps, of sliding planes or of blocks resulting from a rock avalanche process (see Zerathe et al., 2014 and the references herein). To our knowledge, no attempt has been made so far to date the internal scarps of a landslide in order to obtain its kinematics. This paper presents a comprehensive study to constrain the chronology of the large Séchilienne landslide (Western Alps) that affects the right slope of the Romanche valley between 450 m and 1140 m a.s.l. and its relation with the Romanche glacier retreat.

The head scarp and a few polished rock surfaces located in the upper part of the landslide were already locally dated from 23 samples (Le Roux et al., 2009). Application of the CRE

method along the 35 m high head scarp yielded an initiation of the rock-slope failure at 6.4 ± 1.4 ^{10}Be ka and a continuous rock-slope failure activity with a mean head scarp exposure rate of 0.6 cm.yr^{-1} . Glacier retreat at ~ 1100 m a.s.l. was estimated at 16.6 ± 0.6 ^{10}Be ka, with total deglaciation of the valley achieved at least by 13.3 ka. This chronological constraint was however obtained from the Tinée valley located 130 km southeast from the Romanche Valley (Bigot-Cormier et al., 2005).

Here, we sampled rock outcrops within the landslide, at an elevation between 840 and 1140 m a.s.l. with a four-fold objective: (1) to confirm the timing of the failure triggering over the head scarp length, including the main lateral scarp, (2) to assess the vertical glacial retreat rate in the Romanche valley from the dating of polished and striated rock surfaces at lower elevations, (3) to date internal scarps of different sizes and types (valley facing and counter scarps) in order to assess their origin (glacial erosion or gravitational movement) and (4) to get some insight in the landslide kinematics. A total of 63 samples were taken in the upper part of the landslide. In contrast with the major near-vertical head scarp studied by Le Roux et al. (2009), internal scarps were frequently affected by rockfalls, rejuvenating the outcrops and locally providing young ages. The glacially polished outcrops in the landslide often exhibit a wide range of ^{10}Be concentrations, with unexpected low values that suggest that some outcrops have been temporary masked by deposits and subsequently exposed after their erosion. Exposure of rocks to cosmic rays on the Séchilienne slope then turned out to be dependent on multiple processes including the glacial retreat, the erosion of till deposits, the local fall of blocks and gravitational movements. The analysis of this large data set allowed to assess the influence of the different phenomena and to constrain the kinematics of the Séchilienne slope since the Last Glacial Maximum (LGM) around 21 ka (Clarke et al., 2009).

2. Geological setting and dynamics of the landslide

The Séchilienne landslide is located in the southern part of the Belledonne massif (Western Alps) along the East-West trending Romanche valley at 20 km South-East of Grenoble City (Fig.1). This massif, which extends over more 120 km in a N30 direction with a maximum elevation of 3000 m a.s.l., is one of the Paleozoic External Crystalline Massifs of the French Western Alps. It is a part of the Hercynian orogeny that has been overprinted by Alpine shortening and uplift (Guillot et al., 2009). The Paleozoic basement consists of a complex of different metamorphic rocks including gneisses, amphibolites and micaschists unconformably overlain by Mesozoic carbonate sediments and Quaternary deposits (Fig. 1). The incision of the Romanche valley results from alternate activity of water and ice during a succession of Quaternary glaciations including the LGM when the Romanche valley was covered with ice to an elevation of 1200 m a.s.l. (Montjuvent and Winistörfer, 1980).

The present-day landform of the lower Romanche valley shows an important glacial imprint (van der Beek and Bourbon, 2008; Delunel et al., 2010b; Le Roux et al., 2010) such as steep slopes dipping 35° to 40°, overdeepened troughs and glacial deposits. These morphological characteristics suggest a temperate thermal regime for the glacier during the LGM (Lebrouc et al., 2013). Moreover, the right side of the Romanche valley is overlooked by a glacial plateau (Mont Sec plateau in Fig.1) at an elevation higher than 1100 m a.s.l., showing stoss- and-lee surfaces locally covered by peat bogs and moraines. The orientation of grooves and striae is consistent with a north-south trending ice flow on the Mont Sec plateau (Fig. 2). Along the glacial slope, at an elevation lower than 1000 m, rare flow directions are parallel to the Romanche valley direction. The metamorphic rocks in the landslide are affected by three main sets of near-vertical fractures oriented N20, N70 and N110 to N120 (Lebrouc et al., 2013). The N20 fractures are near-parallel to the major late Paleozoic vertical fault so-called the Belledonne Middle Fault (BMF) and their orientation fits the main foliation plane

measured in the micaschists over the slope. The N70 and N110-120 fracture sets correspond to a major regional fracturing network evidenced on both sides of the BMF, in the micaschists and the amphibolites, and is probably inherited from the regional Hercynian and Alpine tectonic framework (Le Roux et al., 2010). In addition, a dense set of N75-oriented short fractures dipping 40-50°S, near parallel to the slope, is observed from the slope surface down to 100 m depth in the Séchilienne landslide (Bièvre et al., 2012).

The Séchilienne landslide has been the subject of multiple investigation campaigns and of monitoring for thirty years (Evrard et al., 1990; Vengeon et al., 1999; Guglielmi et al., 2002; Duranthon et al., 2003; Helmstetter and Garambois, 2010; Le Roux et al., 2011; Cappa et al., 2014). The volume affected by the landslide was estimated to $50\text{-}60 \times 10^6 \text{ m}^3$ with a maximum destabilization depth about 150 m (Le Roux et al., 2011). The global destabilized mass displays medium activity with slow displacement rates ($> 2 \text{ cm.yr}^{-1}$), while, lower in the slope, a frontal mass (The Ruines area in Fig. 2) with a volume of about $3 \times 10^6 \text{ m}^3$ exhibits high velocity reaching a maximum of 100 cm.yr^{-1} and generates frequent rockfalls, as attested by the large scree at the slope foot (Fig. 2).

3. Main morphological features

The Séchilienne slope dominates the right bank of the Romanche valley and three distinct morphological zones can be distinguished from north to south (Figs. 2 and 3a): the near-horizontal preserved glacial plateau, the depleted part of the plateau affected by the landslide and the steeper glacial slope mainly destabilized by recent rockfalls. The preserved glacial plateau (Mont Sec plateau in Figs. 2 and 3) with an elevation of 1140 m a.s.l. has a morphology consisting of alternating North-South elongated depressions carved in micaschist lithology (Figs. 2 and 3a). The rock surfaces are polished, reflecting the erosive activity of the glacier during the last glacial maximum (Fig. 3b), and locally exhibit some

remnant metric glacial striae indicating a southward direction of the ice flow (Fig. 3c). The longest depressions (> 50 m) are infilled by peat bog (Fig. 3b) with a maximum thickness of about 10 m (Legchenko et al., 2011). The plateau is locally covered by moraine deposits of variable thickness, which are mostly preserved in small topographic depressions. These deposits are made of centimeter-size rounded clasts of amphibolite and gneiss in fine-grained matrix. The preserved plateau is delineated to the South by the main landslide scarp (head scarp) of over 1000 m in length, reaching a maximum height of 40 m (Figs. 2, 3a and 3d). Below this head scarp, the second morphological zone is a gentle sloping area situated at an elevation between 1120 and 1000 m a.s.l. This zone, which is interpreted as the depleted glacial plateau, exhibits a series of depressions delineated by a succession of valley-facing scarps and counter scarps reaching 5 to more than 10 m high (Figs. 2, 3a). These structures are oriented N20 and N110 and follow major inherited fracture directions (Fig. 2; Le Roux et al., 2010). The upper near-horizontal surfaces locally exhibit N/S to NE/SW oriented glacial striae (Fig. 3e), in line with the ice flow direction observed on the preserved plateau Mont Sec. These glacial imprint features are often covered and hidden by moraine deposits with a thickness of a few meters. The lower part of the landslide exhibit steep ($> 35^\circ$) convex slopes underlined by a succession of several hundred meters long cliffs, several tens of meters in height and oriented N60°E to N70°E. This feature is interpreted as the lateral steepened rock-slopes of a typical U-shape valley (glacial slope). The cliffs are affected by numerous rockfalls with the development of detrital cones at their foot (Fig. 3g). Despite of this rockfalls activity, relics of near-vertical glacially polished surfaces are visible in the slope (Fig. 3f), with the presence of horizontal grooves several tens of meters in length and of rare near-horizontal striae. In this zone, the grooves and striae indicate an ice flow direction parallel to the Romanche valley (N70) (Fig. 1), which is different from the ice flow orientation observed on the glacial plateau. These glacial features

have been interpreted as resulting from the action of the glaciers of the Isère and Romanche valleys, flowing southward and nearly westward, respectively (Montjuvent and Winistörfer, 1980). This lower part of the landslide is interpreted as an accumulation zone (Vengeon et al., 1999).

In summary, the Séchilienne slope shows both a pronounced glacial morphological imprint and numerous morphological witnesses inherited from the last glacial phase have been preserved on the Mont Sec Plateau and in the slope. After the deglaciation, the slope has been affected by major gravitational movements and rockfalls activity in areas with strong topographic gradient. In an attempt to date both the ice disappearance and the gravitational destabilization, we have sampled quartz on (1) near-horizontal glacially polished surfaces on the Mont Sec plateau (depleted zone), (2) polished surfaces in the steep glacial slope, (3) the main landslide scarp and (4) internal gravitational scarps.

4. In-situ ^{10}Be dating

Cosmic Ray Exposure (CRE) is a geochronological dating method that is based on the accumulation of Terrestrial Cosmogenic Nuclides (TCNs, such as ^{36}Cl , ^{10}Be , or ^{26}Al) in superficial rocks. TCNs are produced within mineral lattice through nuclear reactions between the nucleus of the elements that form the minerals and the incident secondary cosmic ray particles derived from the high-energy galactic cosmic radiation (see a review in Gosse and Phillips, 2001). Because the production rate of these in situ TCNs decreases exponentially with depth (Lal, 1991), their concentrations are directly related to the near-surface exposure history of the analyzed samples and allow determining the exposure ages of the sampled surfaces. In this paper, the dominant endogenous lithology of the bedrock favored the use of the in-situ produced ^{10}Be cosmogenic nuclide within quartz.

4.1. Sampling strategy

Samples for CRE dating were collected from micaschist outcrops hosting quartz veins. The sampling locations are given in Figure 4, while the characteristics of the sampled surfaces are provided in Table 1. Two types of rock surface were sampled: (1) near-vertical scarps of gravitational origin (S1 to S13) and (2) glacially polished surfaces (P14 to P20) (Table 1). In total, 63 quartz-rich samples were collected in order to obtain chronological constrain by CRE dating. This study also takes into account the 23 data presented in Le Roux et al. (2009), marked with an asterisk in Table 1 (S1 to S3, P3, P16 and P17). For consistency, the corresponding ages were recalculated using the most recent update parameters (Heyman, 2014). The new gravitational sampled surfaces (Fig. 4) include 10 scarps (S4 to S14). In total, this study analyses 6 profiles along the main scarp (S1, S2, S3, S4, S5 and S9) and 7 internal scarps of low height (< 10 m) including 3 valley-facing scarps (S10, S11, S12) and 4 counter scarps (S6, S7, S8, S13). All these scarps exhibit steep slope over 70°. The new sampled glacially surfaces (Fig. 4) include 12 flat polished surfaces (P4, P6 to P13, P18, P19 and P20) located at the top of the scarps and 2 vertical profiles along steep (62° and 65°) polished surfaces (P14 and P15). The number of samples per surface varies between 1 and 11, depending on the profile height and the surface type.

All sampled surfaces are located at an elevation ranging from 840 to 1140 m a.s.l.. Indeed, most of the cliffs located below the depleted zone are strongly affected by rockfalls, making it difficult to date their exposure. For both surface types (gravitational and glacial), outcrops exhibiting signs of significant and recent blockfall activity were discarded. However, numerous near-vertical sampled surfaces (8 over 15, see Table 1) exhibit surface morphology with local roughness, which might be caused by blockfalls. This issue will be discussed further in section.

4.2. Nuclide extraction and age calculation

Beryllium-10 (^{10}Be) targets were prepared at the LN2C (Laboratoire National des Nucléides Cosmogéniques, CEREGE, France) following procedures adapted from Brown et al. (1991) and Merchel and Herpers (1999). Crushed rocks were sieved at 200-500 μm and the magnetic grains were separated using a magnetic Frantz separator. Pure quartz was obtained by repeated H_2SiF_6 -HCl etching and then atmospheric ^{10}Be was removed by three sequential dissolutions (each eliminating 10% of the weight) with diluted HF. After addition of 100 μl of an in-house 3.10^{-3} g/g ^9Be carrier solution prepared from deep-mined phenakite (Chmeleff et al., 2010), residual grains were dissolved in 48% HF excess solution. After complete evaporation of the HF, the remaining solutions were purified and beryllium was separated using anion and cation exchange columns. The final precipitate was dried and heated at 900°C to obtain BeO .

Measurements were carried out at the French National AMS facility (Arnold et al., 2013, ASTER, CEREGE, Aix-en-Provence). The $^{10}\text{Be} / ^9\text{Be}$ ratios were calibrated against NIST Standard Reference Material 4325 with an assigned $^{10}\text{Be} / ^9\text{Be}$ ratio of 2.79×10^{-11} (Nishiizumi et al. 2007) and a ^{10}Be half-life of $1.387 \pm 0.012 \cdot 10^6$ yr (Korschinek et al., 2009; Chmeleff et al., 2010).

Ages were calculated using the online Cronus calculator (Balco et al., 2008), considering no erosion rate and a mean rock density of 2.7. The ages have been computed using the scaling scheme of Lal (1991) modified by Stone (2000) and taking into account the effect of paleomagnetic variations (see Balco et al., 2008 for details). The topographic shielding was estimated according to Dunne et al. (1999). We used a global averaged time-dependent

SLHL ^{10}Be production rate of $3.94 \pm 0.20 \text{ at.g}^{-1}.\text{yr}^{-1}$ recently compiled by Heyman (2014) on the basis on 20 site production rates. All calculated ^{10}Be ages are minimum exposure ages.

Analytical uncertainties, involving AMS external error (0.5%), standard reproducibility (Arnold et al., 2013) and chemical blank measurements ($^{10}\text{Be}/^9\text{Be}_{\text{blank}} = 2.46 \pm 0.74 \times 10^{-15}$) have subsequently been propagated through the parameter simulations and are reported within the uncertainties of the resulting exposure ages. All data are presented in Table 2, following the recommendations made by Dunai and Stuart (2009).

4.3. Role of inheritance

A key property of the CRE dating tool is the exponential decrease of the cosmogenic nuclide production rate as a function of depth (Lal, 1991). Within a rock-medium of density of ~ 2.7 , the production rate is known to be reduced to 50%, 20% and $< 5\%$ of the surface production, at 0.5 m, 1 m and 2 m depth, respectively (applying equations and parameters provided in Zerathe et al., 2013 and references therein). This strong attenuation makes the CRE dating a particularly useful and efficient tool to date the exhumation of a large set of geomorphological features, as well as the timing of their recent evolution. Despite the rapid decrease of the production rate below the earth-surface (neutronic component) some specific particles (especially muons), characterized by higher attenuation length, produce a non-negligible accumulation of TCNs at depth as great as 20 m (Braucher et al., 2011). This accumulation of TCNs at depth, prior to the direct-exposure of the studied surface, is called inheritance. In some specific geomorphic configurations (ie. shallow buried faults or landslide scarps), recent studies (Zerathe et al., 2013, 2014) have shown that the inheritance component may represent a non-negligible percentage of the measured cosmogenic nuclide

concentration. Thus, neglecting this parameter for the age calculation may lead to too old apparent ages and incorrect conclusions.

In the case of the Séchilienne landslide, an inherited component of cosmogenic nuclide might be inferred in the upper part of the sampled scarps, due to their shallow burying and, in some case, their low height (Table 1). Unfortunately, the online CRONUS calculator still does not permit to take this parameter into account. Hence, we theoretically calculated the ^{10}Be concentration that would have been inherited along a synthetic scarp, using the classical equation and the parameters of Lal (1991) provided in Zerathe et al. (2013). The calculus was done following a realistic scenario of pre-exposure duration in the studied area, based on constrains from previously published local work (Le Roux et al., 2009). This scenario includes the following hypotheses of : (1) a rock-medium free of inheritance before the local glacier retreat; (2) a pre-exposure duration of 10 ka taking into account a glacier retreat at 16 ka and a landslide activation at 6 ka. An uncertainty of ± 4 ka on the pre-exposure duration; (3) a mean ^{10}Be surface-production rate scaled at 1100 m a.s.l., zero surface erosion and a topographic shielding factor of 1.

The measured ^{10}Be concentrations, and the theoretical curve of ^{10}Be concentration accumulated after a glacier retreat at 16 ka, are plotted against depth in Figure 5a. Most of the measured values are higher than the potentially inherited concentrations under this scenario, indicating that measured ^{10}Be along scarps predominantly comes from direct exposure production. Figure 5b shows the ratio of the theoretically inherited ^{10}Be concentrations and the measured ones for the same scenario, with error bars. The histogram for the same data is drawn in Figure 5c. These figures highlight that the inherited component of ^{10}Be rapidly decreases with depth. Below 3 meters (representing 80% of the measured samples, Fig. 5c), the inheritance part represents less than 10% of the measured one, falling within the age uncertainties (Table 2). Thus, a good confidence can be expected on the

exposure age for the samples below a depth of 3 m, whereas those located in the first 3 m may be affected by non-negligible inheritance.

5. Results

5.1. *Glacially polished surface exposure ages*

The dating results obtained along the glacially polished rock surfaces show a large variability of apparent exposure ages (Table 2). For the glacial Mont Sec plateau, the obtained exposure ages range from 1.9 ± 0.2 ka (P18) to 17.5 ± 1.1 ka (P17), while they vary from 2.4 ± 0.3 ka (P14-2) to 15.4 ± 1 ka (P15-3) on the glacial slope. The two dataset analysis lead to the probability density plots shown in Figures 6 and 7c. On the Mont Sec plateau, two main peaks of higher probability appear, despite the data scattering: one at ca. 8 ka and another at ca. 12 ka (Fig. 6). Along the glacial slope, the probability density analysis of ages over the two profiles P14 and P15 (Figs. 7a and b) reveals two groups of ages, ranging from 2 to 6 ka and from 11 to 16 ka (Fig. 7c).

5.2. *Gravitational surface exposure ages*

The exposure ages obtained along thirteen near-vertical gravitational scarps of the Séchilienne landslide are presented in Figure 8. Ages generally progressively decrease from the scarp top to the base, consistently with the expected downward motion of the landslide mass along the scarps. Few exceptions, including outliers, may reveal more complex histories and will be discussed below. For the main scarps the exposure ages range from 0 to 8 ka (Fig. 8a and Table 2). For the internal scarps exposure ages are significantly younger

(from 1 to 4 ka; Fig. 8b and Table 2), as clearly evidenced by the differences in shape between the two probability density plots (Fig. 8c).

6. Interpretation and discussion

6.1. Deglaciation scenario of the Séchilienne slope

In order to discuss the deglaciation history of the study area, we compare the mean annual air temperature curve (*Tmaa*) from the last 21,000 years (Lebrouc et al., 2013) with the summed probability curves for ^{10}Be ages measured on polished surfaces (Fig. 9). From the temperature curve fluctuations (Fig. 9a), two cold thermal periods are distinguished (labeled A and YD). The A period extends from 21 ka (LGM) to 14.7 ka with *Tmaa* around -8°C . It corresponds to the end of the LGM while the YD period (Younger Dryas) ranges from 13.0 ka to 11.6 ka with *Tmaa* around -10°C .

The exposure ages measured on the polished surfaces on the Mont Sec glacial plateau are very scattered, ranging from about 1.9 to 17.5 ka (Fig. 9b). Source of scattering and presence of outliers are frequent in the field of cosmogenic nuclide dating (Heyman et al., 2011; Balco 2011) and several discrepancy sources have been pointed out. First, some inheritance accumulated during previous exposure history or produced at depth before the exposure event, may lead to an age older than expected (Heyman et al., 2011). That is very unlikely for the Séchilienne slope rocks because of the long-time screening of the temperate Romanche glacier and its associated basal erosion (Lebrouc et al., 2013). In contrast, geological processes may have affected the rock outcrops, making exposure ages significantly younger than the tendency. The two main phenomena are the screening effect of local soil deposits over glacial surfaces (Benson et al, 2004; Briner, 2009; Darnault et al.,

2012) and blockfalls locally rejuvenating near-vertical surfaces (Heymann et al., 2011). On flat surfaces the snow cover can also participate to the screening effect. Indeed, such proton-rich materials strongly attenuate the energy of high-energy neutrons and can reduce the production rate of in-situ ^{10}Be (Delunel et al., 2014). In the Séchilienne area the snow cover might reach few meters during three to six months at the present day (Le Roux et al., 2009), but its thickness and persistence thousands of years ago remain unknown and speculative. All these processes make age interpretations complex in terms of deglaciation timing.

The oldest age is measured on the Mont Sec plateau (17.5 ± 1.1 ka) and it corresponds to the end of the cold period of the LGM (Fig. 9a). Before that time, the plateau was completely covered by several tens of meters of ice (Montjuvent and Winistörfer, 1980), screening cosmic rays and thus resetting the ^{10}Be clock. Because of the absence of nearby high reliefs allowing ice recharge, this value of 17.5 ± 1.1 ka may be assumed to be the minimum age for the plateau deglaciation at ca. 1140 m a.s.l.. This timing is consistent with the regional ice retreat chronology proposed by Delunel (2010), both in the high Romanche valley (13.5 ± 0.4 ^{10}Be ka for an elevation of 2500 m a.s.l.) and in the Isère valley, South of the Chartreuse subalpine zone (15.9 ± 0.4 ^{10}Be ka at 940 m a.s.l.). With this interpretation, all ages younger than about 17.5 ± 1.1 ka are assumed to have experienced an incomplete exposure history due to local screening effects (Heyman et al., 2011). In terms of ^{10}Be concentrations, a deficit of about 80% is found between the oldest sample (P17: 17.5 ka) and the youngest sample (P18: 1.9 ka) in the plateau. As the radioactive decay is negligible (< 1%) over the considered time span (Gosse and Phillips, 2001), this ^{10}Be concentration deficit is directly related to a deficit of same magnitude in the local production rate. Considering a density of ca. 2 g.cm^{-3} for tills (Tailor and Blum, 1995), a reduction of 80% in the ^{10}Be production rate is achieved at ca. 2 m deep (Gosse et Phillips, 2001). Furthermore, the presence of water in such soils (likely saturated) would even increase the phenomena

(Delunel et al, 2014). Morainic relics and several peat bogs with a thickness of several meters are locally covering the Mont Sec plateau (Figs. 1 and 2; Legchenko et al., 2011). Hence, the scenario in which the ^{10}Be production has been hampered by several meters thick sediments seems plausible to explain the anomalously young ages.

The same age scattering is observed over the glacial slope (Fig. 9c), with a succession of old and young ages (Fig. 7b). The irregular slope morphology suggests the regular occurrence of blockfalls, as supported by the presence of block accumulations at cliff foot. For near-vertical surfaces, this supports the hypothesis of a rejuvenation by post-glacial rockfall activity. Considering the oldest age, these results suggest that the glacial slope at an elevation of about 950 m a.s.l. was free of ice at a minimum age of about 15 ± 0.6 ka (Fig. 9c), just at the limit of the cold period A.

The newly acquired and recalculated data sets (23 and 4 exposure ages, respectively, Table 2) allow a consistent deglaciation scenario of the Séchilienne area to be proposed (Fig. 10). Before ca. 17 ka, the valley was entirely filled by the Romanche glacier. The ice recharge of Romanche glacier system was located to the east in the Belledonne high relief area, about 20 km away. Striae on the plateau indicate a southward ice flow direction (Figs. 2 and 10a), compatible with an overflow of the main Romanche glacier (Fig. 1). The glacier retreat at 1140 m over the plateau is dated about 17 ka. Then the down-wastage progressed in the valley with the persistence of a glacial tongue until 13 ka (Fig. 10a). The glacier retreat left a valley floor 150 m below the current level at the front of Séchilienne slope, as shown by geophysical investigation (Le Roux et al., 2010). Since 13 ka (Fig. 10b), the valley has been progressively filled with alluvial deposits from the Romanche River. Along this period, the lateral river erosion may have played an important role, increasing the basal slope steepness. This phenomenon could have been a conditioning factor for the landslide initiation recorded between 8 to 6 ka (Fig. 10c).

6.2. Séchilienne landslide kinematics over the Holocene

Figure 11 shows the exposure ages versus the distance from the top for the main scarps, the valley facing internal scarps and the counter scarps. The dataset shows that ages generally decrease down the scarp, indicating a progressive subsidence of the glacial plateau due to gravitational motion of the Séchilienne slope. Different activity periods can be distinguished on the profiles, consistently with previous kinematic interpretations proposed by Le Roux et al. (2009). On the main scarps, linear fits of the exposure ages over the first ten meters reveal a first period of activity characterized by slow exposure rates (V_1) ranging from 0.9 to 2.6 mm.yr⁻¹ (Fig. 11a). Below, between 10 to 35 m, the exposure rate is higher, about 8 mm.yr⁻¹ (V_2), corresponding to a second period of activity. This change in velocity along the main scarp occurred at ca. 2 ka. The main scarp initiation age can be assessed by the extrapolation of the linear fit (V_1) until the surface, which gives a time window between 8 to 6 ka for the landslide initiation. Determining scarp initiation with accuracy is generally difficult (Zerathe et al., 2014) because measurements in the first meters may be affected by inherited cosmogenic nuclide components and by erosional processes such as blockfalls. For example, the young ages obtain at shallow depth along the S4 and S9 scarps may reflect recent blockfall activity (Fig. 11a).

The exposure rates recorded along the counter scarps are similar to those of the first period of activity (V_1) recorded along the main scarps (Fig. 11b). However their initiation ages are younger and bracketed between 6 to 4 ka. The exposure rates of the valley facing internal scarps are less constrained as they belong on only few ages by profiles (Fig. 11c). Nevertheless, the profile S10 shows accurate exposure rate similar to those determined for the second period of activity (V_2), determined along the main scarps. The profile S11 seems

to indicate a rapid or instantaneous failure. Their initiations seem to be synchronous with the transition (from V_1 to V_2), dated at ca. 2 ka along the main scarps. The internal scarp S12 shows a different behavior with an older period of activity (8 to 6 ka), but measurements were made on two samples only.

6.3. Scenario of the Séchilienne slope deformation

The new chronological constraints (63 over 86) confirm the previous interpretation (Le Roux et al., 2009) that the landslide initiation occurred from 8 to 6 ka, during the Holocene Climatic Optimum, a few thousand years after the main deglaciation of the valley (13 ka). This points out a delay of minimum 5 ka between the glacier retreat and the landslide initiation. This conclusion is consistent with recent finding of Ballantyne et al. (2014) showing that dozen of post-glacial rock-slope failures occurred within ca. 5 ka after deglaciation. This delay is interpreted as a period required to release stress and to progressively propagate failure surfaces. Another factor that may explain this delay is the temporal persistence of thick permafrost layers. The permafrost modeling performed in the Séchilienne slope since the last 21 ka (Lebrouc et al., 2013) suggests that the permafrost expansion damaged significantly the rock-slope. This numerical simulation also shows that the permafrost depth expansion fits well with the landslide thickness deduced from geophysical investigations (Le Roux et al., 2011). However, its disappearance did not trigger the landslide but its persistence probably delays the rupture by mechanically strengthening the slope. Otherwise a climatic control on the landslide triggering and/or the role of a major earthquake cannot be ruled out.

The following scenario is proposed for the deformation of the Séchilienne slope (Fig. 12). From 8 to 6 ka, the failure of the Séchilienne head scarp initiated (Figs. 12a and b),

associated with the subsidence of a part of the Mont Sec plateau at a vertical motion rate of a few mm.yr^{-1} . No or little deformation occurred in the landslide mass during this period. The head scarp was probably connected to a deep rupture surface, the geometry of which will be discussed further (Fig. 12b). The depth of this basal sliding surface is upper-bracketed by the thickness of the deconsolidated mass (about 150 m), determined from geophysical prospecting (Le Roux et al., 2011). At the same time, lower in the slope, the destabilization also affected The Ruines area with the initiation of a main scarp (S4) producing a local subsidence of the area (Fig. 12a).

From 6 to 2 ka (Figs. 12c and d), the counter scarps initiated in the depleted zone at the foot of the head scarp. They recorded a continuous and low subsidence rate at about 2 mm.yr^{-1} , while the destabilized glacial plateau continued subsiding with the same velocity. The initiation of these morpho-structures, which is the first evidence of internal fracturing of the sliding mass, was spatially localized in a thin band of about 100 m at the foot of the head scarp and accommodated the horizontal component of tensional deformation. This indicates that the overall moving mass (depleted plateau) did not only subside but also slide laterally. This result suggests the presence of a continuous deep sliding surface in the upper part of the Séchilienne slope (between 1140 and 850 m), consistent with the deconsolidated mass boundary imaged by large geophysical investigations (Le Roux et al., 2011).

Then, at around 2 ka and up to present (Figs. 12e and f), the vertical motion along the head scarp, which reached 10 m to 15 m, accelerated with an increase in exposure rate up to 8 mm.yr^{-1} . At the same time, two valley facing internal scarps activated with high velocity ($> 8 \text{ mm.yr}^{-1}$). We propose that this reflects the downward propagation of the deformation through the glacial slope in response to the development of a second sliding surface (Fig. 12f), that may enhance the slope destructuration and significant blockfalls activity. The

progressive subsidence of the depleted plateau may generate bulging of the glacial slope associated with toppling and rockfalls (Fig. 12f).

The motions recorded along the valley facing internal scarps were also fast around 8 mm.yr^{-1} , whereas the counter scarps were less active with lower exposure rates (2 mm.yr^{-1}). Interestingly, the kinematics of The Ruines area is synchronous to the acceleration of the Séchilienne head scarp and the global mass movement (compare profiles S4 and S1 in Fig. 11).

At this stage, the geometry of the basal surface rupture can be constrained by recent seismic profiles performed over the slope and two deep boreholes (Le Roux et al., 2011). Considering the lower limit of the deconsolidated mass as the basal rupture surface, the geometry of this deep surface (150 m) exhibits uneven curvature implying multiple rupture planes and internal deformation of the moving mass (Fig. 12f). Of particular interest is the variation in dip of the rupture surface at an elevation of about 850-900 m. Our interpretation is that this listric surface has generated the numerous scarps and counter-scarps in the depleted zone. The locations where these rupture planes daylight in the slope are uncertain due to the lack of morphological expression (Fig. 12f). The current lower limit is fixed by geodetic data and seismic data (Le Roux et al., 2011).

The gravitational kinematics has been continuous and progressive, with several dozen meters of displacement since 8 ka. The internal deformation of the moving mass probably results from the development of a deep uneven basal rupture surface of listric style with multiple branches, and following the geometry of the deconsolidated zone evidenced by geophysical prospecting. This deformation type corresponds to the case of rock compound slide in the classification of Hungr et al. (2014), which is defined as a sliding of a rock mass on a rupture plane consisting of several planes, or a surface of uneven curvature, so that

motion is kinematically possible only if accompanied by significant internal distortion of the moving mass. Horst-and-graben features at the head are typically associated with a listric rupture surface, as observed in the Séchilienne slope or in other deep-seated landslides (e.g. Agliardi et al., 2001; Braathen et al., 2004; Crosta et al., 2014).

7. Conclusion

In this study we bring 63 new CRE ages to decipher the kinematics of the large Séchilienne landslide and its relationship with the deglaciation scenario of the Romanche valley. The previously acquired CRE data (23 samples) were recalculated and combined to the new dataset. Exposure ages acquired on glacially polished surfaces allow two main glacier retreat events to be dated, (i) the early ice melting on the Mont Sec Plateau at 17.5 ka above 1140 m a.s.l., and (ii) the late down-wastage completely achieved in the Romanche valley at ca. 13 ka. The temporal evolution of the slope deglaciation has proved difficult to establish, due to an important scattering of the apparent exposure ages likely influenced by shielding (relict moraines, soil deposits and seasonal snow cover) and rejuvenation (rockfalls) effects on the sampled surfaces.

The gravitational kinematics of the Séchilienne slope is constrained by 12 vertical exposure-age profiles sampled along the main landslide morpho-structures (head scarp, counter scarps and valley facing scarps). We confirm that the landslide initiation occurred from 8 to 6 ka, a few thousand years after the total down-wastage of the valley. The gravitational deformation was initiated along the main scarp (head scarp), leading to a general subsidence of the Mont Sec plateau. At this stage and until 2 ka, the displacement rate recorded along the head scarp was slow (ca. 2 mm.yr⁻¹) in response to a homogeneous motion of the upper part of the Séchilienne slope due to an activation of deep-seated rupture surface with uneven curvature.

The progressive tensional opening at the foot of the head scarp was accommodated by counter scarp activations starting at ca. 6 ka. After 2 ka, the displacement rates increased up to ca. 8 mm.yr⁻¹ in association with the development of internal valley facing scarps. We suggest that this may reflect the downward propagation of the gravitational deformation. The deformation scenario of the Séchilienne slope reflects a progressive rock-slope weakening since 8 ka, associated to a continuous activity of a deep failure surface.

Acknowledgements

This study was supported by the project "ANR-09-RISK-008" (SLAMS) funded by Agence Nationale de la Recherche (France). We thank R. Delunel and an anonymous reviewer for helpful comments that significantly improved the manuscript.

Figure captions.

Fig. 1. Location map of the Séchilienne landslide in the Romanche valley. The location of figure 2 is indicated.

Fig. 2. Geomorphological map of the Séchilienne slope. The study area is subdivided in three main zones with strong glacial imprints: the Mont Sec plateau, the depleted plateau and the glacial slope (see text for details). The zones of active cliffs are shown in yellow. The location of figure 4 is indicated.

Fig. 3. Main morphological features of the Séchilienne slope. (a) Topographic profile of the Séchilienne slope with the three main morphological zones and the location of the photographic views. (b) Glacially polished surface surrounding a peat bog in the preserved Mont Sec Plateau. (c) Example of near-horizontal glacial surface with preserved glacial striae indicating a southward motion (Mont Sec plateau). (d) View of the head scarp. (e) Succession of counter scarps in the depleted glacial plateau. The upper part of the scarp corresponds to the preservation of glacially polished surface. (f) Example of internal valley facing scarp affecting the depleted glacial plateau. (g) Recent rockfall deposits in the footwall of a major cliff. (h) Near-vertical glacially surface with preserved near-horizontal glacial grooves oriented parallel to the Romanche valley (ENE/WSW).

Fig. 4. Digital Model Elevation of the upper part of the Séchilienne slope (between 800 m and 1140 m in elevation). The location of the sampled surfaces is indicated with circles. Gravitational scarps are labeled S1 to S13, while polished glacial surfaces are labeled P14 to P20. The circle color indicates additional information on the surface type (gravitational or glacial) and on the dip orientation (for the internal scarps). Some gravitational scarps exhibit glacially polished surfaces at

their top (half circle in blue). Most glacial surfaces are flat, except P14 and P15 that are located in the glacial slope. The depleted plateau is highlighted in blue.

Fig. 5. (a) ^{10}Be concentrations plotted as a function of depth for all samples. The back curve corresponds to the theoretically expected inherited concentration of ^{10}Be considering a glacier retreat 16 ka ago (see text for details). The upper and lower dashed lines are calculated for a glacier retreat at 12 ka and 20 ka, respectively. (b) For each sample, the percentage of the theoretically inherited ^{10}Be concentration since 16 ka (N_{inh}) against the measured ^{10}Be concentration (N_{10}) is plotted as a function of depth. The error bars take into account ± 4 ka in the timing of the glacier retreat. (c) Frequency/histogram analysis of the same dataset.

Fig. 6. Probability density plot computed for the 16 exposure ages derived from glacially polished surfaces of the Mont Sec plateau. The 16 individual Gaussian curves corresponding to single exposure age are drawn as thin black lines. The thick black curve is the summed probability curve for the 16 exposure ages.

Fig. 7. Exposure age obtained along the glacial slope. (a) and (b), ^{10}Be ages reported along the near-vertical glacially polished surfaces P15 and P14, respectively. (c) Probability density plot showing the 11 individual Gaussian curves (thin black line) and the summed probability curve (thick black line) for the two profiles.

Fig. 8. Vertical profiles of exposure ages obtained along the different gravitational features of the Séchilienne landslide (see location in Fig. 4). (a) Main scarps. (b) Internal scarps. The distinction is made between scarps that are facing to the valley and counter scarps looking upward. (c) On the

right panel, the probability density plots for the main and internal scarps are shown, taking into account the 37 and 22 exposure ages, respectively (see Table 2).

Fig. 9. Mean annual air temperature (T_{maa}) variation of the Séchilienne area (a) since the Late Glacial Maximum (Lebrouc et al., 2013) versus summed probability density curves of the glacial plateau (b) and the glacial slope (c). The two cold periods (A and YD) are indicated in blue and the Holocene Climatic Optimum period is in grey. The timing of the landslide initiation is indicated (8-6 ka). The values 17.5 and 15 ka correspond to maximum ages for glacial retreat on the plateau and on the Séchilienne slope, respectively.

Fig. 10. Deglaciation scenario for the Romanche valley and the initiation of the Séchilienne landslide. (a) Between 21 to 13 ka, progressive Romanche glacier melting. (b) Between 13 to 8 ka, alluvial infill of the Romanche valley. (c) Between 8 to 6, initiation of the landslide along the head scarp. The landslide limit in depth is indicated in red imaged by P-waves seismic velocity (Le Roux et al., 2011).

Fig. 11. Exposure ages versus distance to the top of the gravitational scarps for the (a) main scarps, (b) valley facing scarps and (c) counter scarps. White samples are considered as outliers (see text). $V1$ and $V2$ show the scarp exposure rate for two different periods of activity when sufficient data are available.

Fig. 12. Séchilienne slope evolution presented on map and along a Y-Y' cross section at three different periods from 8 ka to present. (a) and (b) Initiation of the landslide between 8 to 6 ka along the head scarp related to a slow sliding surface activity producing the Mont Sec plateau subsidence. At the same period The Ruines area is destabilized and records a subsidence. (c) and (d) Between 6

to 2 ka, the deformation is still localized on the head scarp and counter scarps slowly developed at its foot, both with an activity at about 2 mm.yr^{-1} . (e) and (f) Between 2 ka to present day the deformation accelerates up to reach 8 mm.yr^{-1} and propagates downward with the development of valley facing scarps activity and rockfalls. For this period, the counter scarps activity generates a highly fractured zone with lower velocity always to the same magnitude around 2 mm.yr^{-1} . The landslide geometry in depth was imaged by P-waves seismic velocity (Le Roux et al., 2011).

Table 1. Morphological characteristics of the sampled surfaces and number of samples. S: Gravitational scarp; P: Glacially polished surface. Glacially polished surfaces with the same number (e.g. P13) as gravitational surfaces are located at the top of the scarp (e.g. S13). Counter scarps are facing north while the valley facing scarps are dipping to the south. The data from Le Roux et al. (2009) are marked with an asterisk (S1 to S3, P3, P16 and P17).

Table 2. Analytical CRE results of the Séchilienne site, with S: Gravitational scarp, P: Glacially polished surface. The data from Le Roux et al. (2009) are marked with an asterisk.

References

- Agliardi, F., Crosta, G., Zanchi, A., 2001. Structural constraints on deep-seated slope deformation kinematics. *Engineering Geology* 59 (1), 83–102.
- Anderson, R.S., Anderson, S.P., 2012. *The Mechanics and Chemistry of Landscapes*, Cambridge University Press.
- Anderson, R. S., Molnar, P., Kessler, M.A., 2006. Features of glacial valley profiles simply explained. *Journal of Geophysical Research*, 111, F01004, doi:10.1029/2005JF000344.
- Arnold, M., Aumaître, G., Bourlès, D.L., Keddaddouche, K., Braucher, R., Finkel, R.C., Nottoli, E., Benedetti, L., Merchel, S., 2013. The French accelerator mass spectrometry facility ASTER after 4 years: status and recent developments on ^{36}Cl and ^{129}I Nuclear Instruments and Methods in Physics Research B 294, 24–28.
- Augustinus, P.C., 1995. Glacial valley cross-profile development: the influence of in situ rock stress and rock mass strength, with examples from the southern Alps, New Zealand. *Geomorphology* 14, 87–97.
- Balco, G., 2011. Contributions and unrealized potential contributions of cosmogenic-nuclide exposure dating to glacier chronology 1990–2010. *Quaternary Science Reviews* 30, 3–27.
- Balco, G., Stone, J.O., Lifton, N.A., Dunai, T.J., 2008. A complete and easily accessible means of calculation surface exposure ages or erosion rates from ^{10}Be and ^{26}Al measurements. *Quaternary Geochronology* 3, 174–195.
- Ballantyne, C.K., 2002. Paraglacial geomorphology. *Quaternary Science Reviews* 21, 1935–2017.
- Ballantyne, C.K., Sanderman, G.F., Stone, J.O., Wilson, P., 2014. Rock-slope failure following Late Pleistocene deglaciation on tectonically stable mountainous terrain. *Quaternary Science Reviews* 86, 144–157.

Braathen, A., Blikra, L.H., Berg, S.S., Karlsen, F., 2004. Rock-slope failures in Norway; type, geometry, deformation mechanisms and stability. *Norwegian Journal of Geology* 84, 67–88.

Benson, L., Madole, R., Phillips, W., Landis, G., Thomas, T., Kubik, P., 2004. The probable importance of snow and sediment shielding on cosmogenic ages of north-central Colorado Pinedale and pre-Pinedale moraines. *Quaternary Science Reviews* 23, 193-206.

Bièvre, G., Kasperski, J., Pothérat, P., 2012. Séchilienne - Programme de reconnaissances. Interprétation géologique des sondages. Technical report CETE de Lyon 40320-1 and 41106-1, CETE de Lyon, Lyon, France.

Bigot-Cormier, F., Braucher, R., Bourlès, D., Guglielmi, Y., Dubar, M., Stéphan, J.F., 2005. Chronological constraints on processes leading to large active landslides. *Earth and Planetary Science Letters* 235, 141–150.

Blair, R.W., 1994. Moraine and valley wall collapse due to rapid deglaciation in Mount Cook National Park, New Zealand. *Mountain Research and Development* 14, 347–358.

Braucher, R., Merchel, S., Borgomano, J., Bourlès, D., 2011. Production of cosmogenic radionuclides at great depths: a multi element approach. *Earth and Planetary Science Letters* 309, 1–9.

Brown, E.T., Edmond, J.M., Raisbeck, G.M., Yiou, F., Kurz, M.D., Brook, E.J., 1991. Examination of surface exposure ages of moraines in Arena Valley, Antarctica, using in situ produced ^{10}Be and ^{26}Al . *Geochimica et Cosmochimica Acta* 55, 2269–2283.

Briner, J P., 2009. Moraine pebbles and boulders yield indistinguishable ^{10}Be ages: a case study from Colorado, USA. *Quaternary Geochronology* 4, 299-305.

Cappa, F., Guglielmi, Y., Viseur, S., Garambois, S., 2014. Deep fluids can facilitate rupture of slow-moving giant landslides as a result of stress transfer and frictional weakening. *Geophysical Research Letters* 41, 1–6, doi:10.1002/2013GL058566

Chmeleff, J., von Blanckenburg, F., Kossert, K., Jakob, J., 2010. Determination of the ^{10}Be half-life by multicollector ICP-MS and liquid scintillation counting. *Nuclear Instruments and Methods in Physics Research B* 268 (2), 192–199.

- Clark, P.U., Dyke, A.S., Shakun, J.D., Carlson, A.E., Clark, J., Wohlfarth, B., Mitrovica, J.X., Hostetler, S.W., McCabe, A.M., 2009. The last glacial maximum. *Science* 325, 710–714.
- Cossart, E., Braucher, R., Fort, M., Bourlès, D.L., Carcaillet, J., 2008. Slope instability in relation to glacial debuitressing in alpine areas (upper durance catchment, southeastern France): Evidence from field data and ^{10}Be cosmic ray exposure ages. *Geomorphology* 95, 3–26.
- Crosta, G., Di Prisco, C., Frattini, P., Frigerio, G., Castellanza, R., Agliardi, F. (2014). Chasing a complete understanding of the triggering mechanisms of a large rapidly evolving rockslide. *Landslides* 11(5), 747–764.
- Cruden, D.M., Hu, X.Q., 1993. Exhaustion and steady states models for predicting landslides hazards in the Canadian Rocky Mountains. *Geomorphology* 8, 279–285.
- Darnault, R., Rolland, Y., Braucher, R., Bourlès, D., Revel, M., Sanchez, G., Bouissou, S., 2012. Timing of the last deglaciation revealed by receding glaciers at the Alpine-scale: impact on mountain geomorphology. *Quaternary Science Reviews* 31, 127–142.
- Delunel, R., 2010. Evolution géomorphologique du massif des Ecrins-Pelvoux depuis le Dernier Maximum Glaciaire. Apports des nucléides cosmogéniques produits in-situ. *Géomorphologie*. PhD Thesis, Université Joseph-Fourier - Grenoble I.
- Delunel, R., Hantz, D., Braucher, R., Bourlès, D.L., Schoeneich, P., Deparis, J., 2010a. Surface exposure dating and geophysical prospecting of the Holocene Lauvitel rock slide (French Alps). *Landslide* 7, 393–400.
- Delunel, R., van der Beek, P., Carcaillet, J., Bourlès, D., Valla, P., 2010b. Frost-cracking control on catchment denudation rates: Insights from in situ produced ^{10}Be concentrations in stream sediments (Ecrins–Pelvoux massif, French Western Alps). *Earth and Planetary Science Letters* 293, 72–83.
- Delunel, R., Bourlès, D., van der Beek, P., Schlunegger, F., Leya, I., Masarik, J., Paquet, E., 2014. Snow shielding factors for cosmogenic nuclide dating inferred from long-term neutron detector monitoring. *Quaternary Geochronology* 24, 16–26.

Dunforth, M., Anderson, R.S., Ward, D., Stock, G.M., 2010. Bedrock fracture control of glacial erosion processes and rates. *Geology* 28, 423-426.

Dunai, T., Stuart, F.M., 2009. Reporting of cosmogenic nuclide data for exposure age and erosion rate determinations. *Quaternary Geochronology* 4, 437-440.

Dunne, A., Elmore, D., Muzicar, P., 1999. Scaling of cosmogenic nuclide production rates for geometric shielding and attenuation at depth on sloped surfaces. *Geomorphology* 27, 3-11.

Duranthon, J.P., Effendiantz, L., Memier, M., Previtali, I., 2003. Apport des méthodes topographiques et topométriques au suivi du versant rocheux instable des ruines de Séchilienne. *Revue XYZ* 94, 31-38.

Erismann, T.H., Abele, G., 2001. *Dynamics of Rockslides and Rockfalls*. Springer-Verlag, Berlin. 316 pp.

Evans, S.G., Clague, J.J., 1994. Recent climatic change and catastrophic geomorphic processes in mountain environments. *Geomorphology* 10, 107-128.

Evrard, H., Gouin, T., Benoit, A., Duranthon, J.P., 1990. Séchilienne, risques majeurs d'éboulements en masse; point sur la surveillance du site. *Bulletin de Liaison des Ponts et Chaussées* 165, 7-16.

Gosse, J.C., Phillips, F.M., 2001. Terrestrial in situ cosmogenic nucleides: theory and application. *Quaternary Science Reviews* 20, 1475-1560.

Guglielmi, Y., Vengeon, J.M., Bertrand, C., Mudry, J., Follacci, J.P., Giraud, A., 2002. Hydrogeochemistry: an investigation tool to evaluate infiltration into large moving rock masses (case study of La Clapière and Séchilienne alpine landslides). *Bulletin of Engineering Geology and the Environment* 61, 311-324.

Guillot, S., Di Paola, S., Ménot, R.P., Ledru, P., Spalla, M.I., Gosso, G., Schwartz, S., 2009. Suture zones and importance of strike-slip faulting for Variscan geodynamic reconstructions of the External Crystalline Massifs of the western Alps. *Bulletin de la Société Géologique de France* 180, 483-500.

Harbor, J. M., 1992. Numerical modeling of the development of U-shaped valleys by glacial erosion. *Geological Society of American Bulletin* 104(10), 1364–1375.

Harbor, J. M., 1995. Development of glacial-valley crosssections under conditions of spatially variable resistance to erosion. *Geomorphology* 14, 99–107.

Helmstetter, A. and Garambois, S., 2010. Seismic monitoring of Séchilienne rockslide (French Alps): Analysis of seismic signals and their correlation with rainfalls, *Journal of Geophysical Research*, 115, F03016, doi:10.1029/2009JF001532

Herman, F., Braun, J., 2008. Evolution of the glacial landscape of the Southern Alps of New Zealand: Insights from a glacial erosion model. *Journal of Geophysical Research* 113, F02009, doi:10.1029/2007JF000807.

Hippolyte, J.C., Brocard, G., Tardy, M., Nicoud, G., Bourlès, D., Braucher, R., Ménéard, G., Souffaché, B., 2006. The recent fault scarps of the Western Alps (France): Tectonic surface ruptures or gravitational sacking scarps? A combined mapping, geomorphic, levelling, and ^{10}Be dating approach. *Tectonophysics* 418, 255–276.

Holm, K., Bovis, M., Jakob, J., 2004. The landslide response of alpine basins to post-Little Ice Age glacial thinning and retreat. *Geomorphology* 57, 201–216

Hormes, A., Ivy-Ochs, S., Kubik, P.W., Ferreli, L., Michetti, A.L., 2008. ^{10}Be exposure ages of a rock avalanche and a late glacial moraine in Alta Valtellina, Italian Alps. *Quaternary International* 190, 136–145.

Heyman, J., Stroeven, A.P., Harbor, J.M., Caffee, M.W., 2011. Too young or too old: evaluating cosmogenic exposure dating based on an analysis of compiled boulder exposure ages. *Earth and Planetary Science Letters* 302, 71-80.

Heyman, J., 2014. Paleoglaciation of the Tibetan Plateau and surrounding mountains based on exposure ages and ELA depression estimates. *Quaternary Science Reviews*, 91, 30-41.

Hungr, O., Leroueil, S., Picarelli, L., 2014. The Varnes classification of landslide types, an update. *Landslides* 11, 167–194.

- Ivy-Ochs, S., Heuberger, H., Kubik, P.W., Kerschner, H., Bonani, G., Frank, M., Schlüchter, C., 1998. The age of the Köfels event: relative, ^{14}C and cosmogenic isotope dating of an early Holocene landslide in the Central Alps (Tyrol, Austria). *Z. Gletsch. kd. Glazialgeol.* 34/1, 57–68.
- Ivy-Ochs, S., Poschinger, A.v., Synal, H.-A., Maisch, M., 2009. Surface exposure dating of the Flims landslide, Graubünden, Switzerland. *Geomorphology* 103, 104–112.
- Kelly, M.A., Buoncristiani, J.F., Schluchter, C., 2004. Are construction of the last glacial maximum (LGM) ice-surface geometry in the western Swiss Alps and contiguous Alpine regions in Italy and France. *Eclogae Geologicae Helvetiae* 97, 57–75.
- Korschinek, G., Bergmaier, A., Faestermann, T., Gerstmann, U.C., Knie, K., Rugel, G., Wallner, A., Dillmann, I., Dollinger, G., von Gostomski Lierse, Ch., Kossert, K., Maitia, M., Poutivtsev, M., Remmert, A., 2009. A new value for the half-life of ^{10}Be by heavy-ion elastic recoil detection and liquid scintillation counting. *Nuclear Instruments and Methods in Physics Research B* 268 (2), 187–191.
- Korup, O., 2008. Rock type leaves topographic signature in landslide-dominated mountain ranges. *Geophysical Research Letters* 35, L11402. doi:10.1029/2008GL034157.
- Krabbendam, M., Glasser, N.F., 2011. Glacial erosion and bedrock properties in NW Scotland: Abrasion and plucking, hardness and joint spacing. *Geomorphology* 130, 374–383.
- Lal, D., 1991. Cosmic ray labeling of erosion surfaces: in situ nuclide production rates and erosion models. *Earth and Planetary Science Letters* 104, 424–439.
- Lebrouc, V., Schwartz, S., Baillet, L., Jongmans, D., Gamond, J.F., 2013. Permafrost extension modeling in a rock slope since the Last Glacial Maximum : application to the large Séchilienne landslide (French Alps). *Geomorphology* 198, 189–200.
- Legchenko, A., Clément, R., Garambois, S., Maury, E., Mic, L.M., Laurent, J.P., Desplanque, C., Guyard, H., 2011. Investigating water distribution in the Luitel Lake peat bog using MRS, ERT and GPR. *Near Surface Geophysics* 9, 201–209.

- Le Roux, O., Jongmans, D., Kaperski, J., Schwartz, S., Potherat, P., Lebruc, V., Lagabrielle, R., Meric, O., 2011. Deep geophysical investigation of the large Séchilienne landslide (western Alps, France) and calibration with geological data. *Engineering Geology* 120, 18–31.
- Le Roux, O., Schwartz, S., Gamond, J.F., Jongmans, D., Bourlès, D., Braucher, R., Mahaney, W., Carcaillet, J., Leanni, L., 2009. CRE dating on the head scarp of a major landslide (Séchilienne, French Alps), age constraints on Holocene kinematics, *Earth and Planetary Science Letters* 280, 236–245.
- Le Roux, O., Schwartz, S., Gamond, J.F., Jongmans, D., Tricart, P., Sébrier, M., 2010. Interaction between tectonic and erosion processes on the morphogenesis of an alpine valley: geological and geophysical investigations in the lower Romanche valley (Belledonne massif, western Alps). *International Journal of Earth Sciences* 99, 427–441.
- MacGregor, K.C., R.S. Anderson, S.P. Anderson, Waddington, E.D., 2000. Numerical simulations of longitudinal profile evolution of glacial valleys. *Geology* 28, 1031–1034.
- McColl, S.T., 2012. Paraglacial rock-slope stability. *Geomorphology* 153-154, 1–16.
- Martin, S., Campedel, P., Ivy-Ochs, S., Viganò, A., Alfimov, V., Vockenhuber, C., Rigo, M., 2014. Lavini di Marco (Trentino, Italy): ^{36}Cl exposure dating of a polyphase rock avalanche. *Quaternary Geochronology* 19, 106-116.
- Merchel, S., Herpers, U., 1999. An update on radiochemical separation techniques for the determination of long-lived radionuclides via accelerator mass spectrometry. *Radiochimica Acta* 84, 215–219.
- Montgomery, D.R., 2002. Valley formation by fluvial and glacial erosion. *Geology* 30, 1047–1050.
- Montjuvent, G., Winistörfer, J., 1980. Glaciers quaternaires dans les Alpes franco-suissees et leur piedmont. *Géologie Alpine* 56, 251-282.
- Nishiizumi, K., Imamura, M., Caffee, M., Southon, J., Finkel, R., McAnich, J., 2007. Absolute calibration of ^{10}Be AMS standards. *Nuclear Instruments and Methods in Physics Research B* 258, 403–413.

- Ostermann, M., Sanders, D., Ivy-Ochs, S., Alfimov, V., Rockenschaub, M., Römer, A., 2012. Early Holocene (8.6 ka) rock avalanche deposits, Obernberg valley (Eastern Alps): landform interpretation and kinematics of rapid mass movement. *Geomorphology* 171-172, 83–93.
- Prager, C., Ivy-Ochs, S., Ostermann, M., Synal, H.A., Patzelt, G., 2009. Geology and radiometric ^{14}C , ^{36}Cl and Th-/U-dating of the Fernpass rockslide (Tyrol, Austria). *Geomorphology* 103, 93–103.
- Salcher B.C., Kober F., Kissling E. and Willett S.D., 2014. Glacial impact on short-wavelength topography and long-lasting effects on the denudation of a deglaciated mountain range, *Global and Planetary Change* 115, 59–70.
- Sanchez, G., Rolland, Y., Corsini, M., Braucher, R., Bourlès, D., Arnold, M. Aumaître, G., 2009. Relationships between tectonics, slope instability and climate change: cosmic ray exposure dating of active faults, landslides and glacial surfaces in the SW Alps. *Geomorphology* 117, 1–13.
- Seijmonsbergen, A.C., Woning, M.P., Verhoef, P.N.W., de Graaff, L.W.S., 2005. The failure mechanism of a Late Glacial Sturzstrom in the Subalpine Molasse (Leckner Valley, Vorarlberg, Austria). *Geomorphology* 66, 277–286.
- Stone, J.O., 2000. Air pressure and cosmogenic isotope production. *Journal of Geophysical Research* 105 (B10), 23753–23759.
- Taylor, A., Blum, J.D., 1995. Relation between soil age and silicate weathering rates determined from the chemical evolution of a glacial chronosequence. *Geology* 23, 979-982.
- van der Beek, P., Bourbon, P., 2008. A quantification of the glacial imprint on relief development in the French western Alps. *Geomorphology* 97, 52–72.
- Vengeon, J.M., Giraud, A., Antoine, P., Rochet, L., 1999. Analysis of the deformation and toppling of rock slopes in crystallophyllian terrain. *Canadian Geotechnical Journal* 36, 1123–1136.
- Zerathe, S., Braucher, R., Lebourg, T., Bourlès, D., Manetti, M., Leanni, L., 2013. Dating chert (diagenetic silica) using in-situ produced ^{10}Be : possible complications revealed

through the comparison with ^{36}Cl applied on coexisting limestone. *Quaternary Geochronology* 17, 81-93.

Zerathe, S., Lebourg T., Braucher R., Bourles D., 2014. Mid-Holocene cluster of large-scale landslides revealed in the Southwestern Alps by Cl-36 dating. Insight on an Alpine-scale landslide activity. *Quaternary Science Reviews* 90, 106–127.

ACCEPTED MANUSCRIPT

Table 1

Sampled surface	X(m) ^a	Y(m) ^a	Elevation (m a.s.l.)	Geomorphological zone	Mean slope dip (°)	Slope facing	Surface roughness	Height (m)	Number of samples
Gravitational surface									
S2*	720730	4994255	1128.0	Main scarp	90	Valley facing	rough	28.0	4
S3*	720495	4994160	1071.0	Main scarp	78	Valley facing	rough	26.5	5
S4	721028	4996286	868.2	Main scarp	75	Valley facing	smooth	30.5	10
S5	720271	4994113	1034.3	Main scarp	76	Valley facing	smooth	8.0	4
S6	720743	4994190	1114.0	Depleted plateau	82	Counter scarp	rough	8.5	5
S7	720727	4994179	1118.0	Depleted plateau	73	Counter scarp	smooth	8.0	5
S8	720725	4994178	1120.2	Depleted plateau	78	Counter scarp	smooth	6.5	4
S9	720820	4994131	1119.6	Main scarp	80	Valley facing	rough	14.0	5
S10	720771	4994083	1081.9	Depleted plateau	73	Valley facing	rough	9.5	5
S11	720783	4994109	1105.2	Depleted plateau	77	Valley facing	rough	6.4	3
S12	720788	4994151	1111.6	Depleted plateau	72	Valley facing	rough	8.0	3
Glacially polished surface									
P3*	720490	4994160	1080.0	Main scarp	0	-	smooth	0	1
P4	721040	4996281	873.1	Main scarp	0	-	smooth	0	1
P6	720743	4994190	1115.0	Depleted plateau	0	-	smooth	0	1

P7	720727	4994179	1120.0	Depleted plateau	0	-	smooth	0	1
P8	720725	4994178	1122.0	Depleted plateau	0	-	smooth	0	1
P9	720820	4994131	1120.0	Main scarp	0	-	smooth	0	1
P10	720771	4994083	1084.0	Depleted plateau	0	-	smooth	0	1
P11	720783	4994109	1108.0	Depleted plateau	0	-	smooth	0	1
P12	720788	4994151	1115.0	Depleted plateau	0	-	smooth	0	1
P13	720769	4994176	1112.0	Depleted plateau	0	-	smooth	0	1
P14	720620	4993807	953.0	Glacial slope	62	Valley facing	rough	29.5	8
P15	720423	4993795	958.0	Glacial slope	65	Valley facing	smooth	35.5	3
P16*	720720	4994560	1120.0	Preserved plateau	0	-	smooth	0	2
P17*	720725	4994175	1121.0	Depleted plateau	0	-	smooth	0	1
P18	720277	4990920	1023.0	Depleted plateau	0	-	smooth	0	1
P19	720256	4990840	1015.0	Depleted plateau	0	-	smooth	0	1
P20	720768	4994151	1117.0	Depleted plateau	0	-	smooth	0	1

^a Location in WGS84 - UTM31N

Table 2

Sample	X ^a	Y ^a	Elevation	Z ^b	D ^c	T ^d	St ^e	Scaled production rates		¹⁰ Be concentration ^f			Ages ^g	
	(m)	(m)	(m a.s.l.)	(m)	(m)	(cm)		(atoms/g/yr)	(atoms/g)	N_{10}	σN_{10}	T min	Ext. σT	Int. σT
S1-1*	720830	4994190	1139.0	2.1	2.2	2.0	0.50	5.05	0.263	30408	1804	5.7	0.5	0.3
S1-2*	720830	4994190	1137.0	4.1	4.3	2.0	0.50	5.04	0.263	33962	4699	6.4	0.9	0.9
S1-3*	720830	4994190	1131.8	9.3	9.7	2.0	0.50	5.02	0.263	20542	1794	3.9	0.4	0.3
S1-4*	720830	4994190	1125.0	16.1	16.8	2.0	0.50	4.99	0.262	11061	901	2.1	0.2	0.2
S1-5*	720830	4994190	1124.0	17.1	17.8	2.0	0.50	4.99	0.262	7740	1103	1.5	0.2	0.2
S1-6*	720830	4994190	1123.6	17.5	18.2	2.0	0.50	4.99	0.262	10392	1581	2.0	0.3	0.3
S1-7*	720830	4994190	1121.0	20.1	20.9	2.0	0.50	4.98	0.262	11695	1236	2.3	0.3	0.2
S1-8*	720830	4994190	1119.3	21.8	22.7	2.0	0.50	4.97	0.262	6982	2023	1.4	0.4	0.4
S1-9*	720830	4994190	1116.0	25.1	26.1	2.0	0.49	4.86	0.261	5982	864	1.2	0.2	0.2
S1-10*	720830	4994190	1112.3	28.8	30.0	2.0	0.48	4.74	0.261	3370	970	0.7	0.2	0.2
S1-11*	720830	4994190	1109.0	32.1	34.4	2.0	0.47	4.63	0.261	1730	722	0.4	0.2	0.1
S2-1*	720730	4994255	1128.0	2.0	2.0	2.0	0.45	4.51	0.262	15444	1718	3.3	0.4	0.4
S2-2*	720730	4994255	1126.5	3.5	3.5	2.0	0.45	4.50	0.262	6915	1271	1.5	0.3	0.3
S2-3*	720730	4994255	1125.5	4.5	4.5	2.0	0.45	4.50	0.262	7576	2628	1.6	0.6	0.6

S2-4*	720730	4994255	1120.0	10.0	10.0	2.0	0.55	5.47	0.262	17978	2196	3.2	0.4	0.4
P3*	720490	4994160	1080.0	-	-	2.0	0.93	8.96	0.258	139574	4028	15.1	0.9	0.4
S3-1*	720495	4994160	1071.0	8.3	8.5	2.0	0.55	5.26	0.257	29833	3334	5.4	0.7	0.6
S3-2*	720495	4994160	1066.5	12.8	13.1	2.0	0.50	4.77	0.257	6127	1509	1.2	0.3	0.3
S3-3*	720495	4994160	1062.5	16.8	17.2	2.0	0.50	4.75	0.257	9194	2534	1.9	0.5	0.5
S3-4*	720495	4994160	1057.5	21.8	22.3	2.0	0.50	4.73	0.256	10617	1931	2.2	0.4	0.4
P4	721040	4996281	873.1	-	-	1.0	0.99	8.18	0.242	120202	4351	14.2	0.9	0.5
S4-1	721028	4996286	868.2	1.2	1.3	2.0	0.59	4.78	0.241	10957	1645	2.2	0.4	0.3
S4-2	721028	4996286	866.7	2.7	2.8	3.0	0.59	4.73	0.240	6621	1042	1.3	0.2	0.2
S4-3	721040	4996286	864.0	5.4	5.6	1.5	0.59	4.78	0.241	17694	1633	3.5	0.4	0.3
S4-4	721040	4996286	862.4	7.0	7.3	1.5	0.59	4.77	0.240	13310	1389	2.7	0.3	0.3
S4-5	721040	4996286	861.4	8.0	8.3	3.5	0.59	4.69	0.239	8916	1346	1.8	0.3	0.3
S4-6	721028	4996286	857.3	12.1	12.6	2.0	0.59	4.73	0.240	4837	796	1.0	0.2	0.2
S4-7	721034	4996286	855.1	14.3	14.9	2.5	0.59	4.71	0.239	2161	679	0.5	0.1	0.1
S4-8	721040	4996286	852.6	16.8	17.5	1.5	0.59	4.74	0.240	962	679	0.2	0.1	0.1
S4-9	721028	4996286	849.1	20.3	21.1	3.0	0.59	4.66	0.239	1445	518	0.3	0.1	0.1
S5-1	720271	4994113	1034.3	0.8	0.8	1.5	0.57	5.36	0.255	40448	2292	7.2	0.5	0.4
S5-2	720271	4994113	1033.8	1.3	1.3	4.0	0.52	4.78	0.253	27192	2503	5.4	0.6	0.5

S5-3	720271	4994113	1030.8	4.3	4.4	2.0	0.52	4.84	0.254	7465	1521	1.5	0.3	0.3
S5-4	720271	4994113	1029.1	6.0	6.2	2.5	0.52	4.82	0.254	11782	2327	2.3	0.5	0.5
P6	720743	4994190	1115.0	-	-	2.1	0.97	9.59	0.261	57674	2873	5.8	0.4	0.3
S6-1	720743	4994190	1114.0	1.0	1.0	4.5	0.64	6.28	0.260	21427	1661	3.3	0.3	0.3
S6-2	720743	4994190	1112.5	2.5	2.5	2.5	0.64	6.37	0.261	20139	1597	3.1	0.3	0.2
S6-3	720743	4994190	1111.1	3.9	3.9	2.0	0.64	6.39	0.261	21210	1644	3.2	0.3	0.2
S6-4	720743	4994190	1109.2	5.8	5.9	2.0	0.64	6.38	0.261	11095	1153	1.7	0.2	0.2
P7	720727	4994179	1120.0	-	-	1.5	0.98	9.81	0.262	112327	4370	11.1	0.7	0.4
S7-1	720727	4994179	1118.0	2.0	2.1	2.0	0.71	7.04	0.261	28452	1901	3.9	0.3	0.3
S7-2	720727	4994179	1117.0	3.0	3.1	3.0	0.71	6.98	0.261	21715	2121	3.0	0.3	0.3
S7-3	720727	4994179	1116.1	3.9	4.1	2.0	0.71	7.03	0.261	17399	2122	2.4	0.3	0.3
S7-4	720727	4994179	1112.8	7.2	7.5	2.5	0.71	6.99	0.261	8712	1161	1.2	0.2	0.2
P8	720725	4994178	1122.0	-	-	1.5	0.99	9.87	0.262	87628	3081	8.6	0.5	0.3
S8-1	720725	4994178	1120.2	1.8	1.8	1.5	0.63	6.31	0.262	22969	1994	3.5	0.4	0.3
S8-2	720725	4994178	1119.4	2.6	2.7	2.0	0.63	6.28	0.262	8846	1121	1.4	0.2	0.2
S8-3	720725	4994178	1117.3	4.7	4.8	1.5	0.63	6.30	0.262	7554	1169	1.2	0.2	0.2
P9	720820	4994131	1120.0	-	-	2.0	0.96	9.53	0.262	76852	4241	7.8	0.6	0.4
S9-1	720820	4994131	1119.6	0.4	0.4	4.5	0.50	4.88	0.260	22046	1576	4.3	0.4	0.3

S9-2	720820	4994131	1116.6	3.4	3.3	1.0	0.50	5.00	0.262	18860	1542	3.6	0.3	0.3
S9-3	720820	4994131	1114.2	5.8	5.7	1.0	0.50	4.99	0.262	24122	1964	4.6	0.4	0.4
S9-4	720820	4994131	1112.8	7.2	7.1	4.5	0.50	4.85	0.260	17802	1907	3.5	0.4	0.4
S9-5	720820	4994131	1111.6	8.4	8.2	2.0	0.50	4.94	0.261	12803	1327	2.5	0.3	0.3
P10	720771	4994083	1084.0	-	-	2.0	0.92	8.91	0.259	72389	3149	7.8	0.5	0.3
S10-1	720771	4994083	1081.9	2.1	2.2	4.5	0.65	6.19	0.257	10954	1563	1.7	0.3	0.2
S10-2	720771	4994083	1080.9	3.1	3.2	1.0	0.65	6.36	0.259	11531	1300	1.8	0.2	0.2
S10-3	720771	4994083	1079.0	5.0	5.2	2.0	0.65	6.26	0.258	9574	1417	1.5	0.2	0.2
S10-4	720771	4994083	1076.8	7.2	7.5	1.0	0.65	6.30	0.259	7413	1317	1.1	0.2	0.2
P11	720783	4994109	1108.0	-	-	4.5	0.86	8.34	0.259	95054	3530	11.0	0.7	0.4
S11-1	720783	4994109	1105.2	2.8	2.9	2.0	0.42	4.10	0.26	9574	1417	2.2	0.3	0.3
S11-2	720783	4994109	1103.9	4.1	4.2	2.5	0.42	4.08	0.26	10345	1456	2.4	0.4	0.3
P12	720788	4994151	1115.0	-	-	1.0	0.89	8.98	0.262	84041	3083	9.0	0.6	0.3
S12-1	720788	4994151	1111.6	3.4	3.6	1.0	0.52	5.22	0.262	47718	2916	8.6	0.7	0.5
S12-2	720788	4994151	1109.4	5.6	5.9	4.5	0.52	5.06	0.259	30269	3498	5.7	0.7	0.7
P13	720769	4994176	1112.0	-	-	2.1	0.98	9.72	0.261	126916	1402	12.7	0.7	0.1
S13-1	720769	4994176	1110.2	1.8	1.9	4.5	0.45	4.33	0.259	12617	1355	2.8	0.3	0.3
S13-2	720769	4994176	1108.4	3.6	3.7	2.5	0.45	4.40	0.26	11553	1382	2.5	0.3	0.3

S13-3	720769	4994176	1107.0	5.0	5.2	1.0	0.45	4.45	0.261	8750	1272	1.9	0.3	0.3
P14-0	720620	4993807	953.0	-	-	1.5	0.99	8.61	0.248	98462	4365	11.1	0.7	0.5
P14-1	720620	4993807	950.2	2.8	3.2	2.5	0.52	4.53	0.247	22652	1654	4.7	0.4	0.3
P14-2	720620	4993807	948.6	4.4	5.0	2.0	0.52	4.55	0.247	11425	1316	2.4	0.3	0.3
P14-3	720620	4993807	945.2	7.8	8.9	3.0	0.52	4.50	0.246	54590	2555	11.5	0.8	0.5
P14-4	720620	4993807	939.1	13.9	15.8	2.1	0.52	4.51	0.246	27502	2120	5.8	0.5	0.4
P14-5	720620	4993807	936.5	16.5	18.7	4.5	0.52	4.41	0.245	15004	1754	3.2	0.4	0.4
P14-6	720620	4993807	930.7	22.3	25.3	2.5	0.52	4.46	0.245	43381	2443	9.2	0.7	0.5
P14-7	720620	4993807	929.2	23.8	27.0	4.5	0.52	4.39	0.244	26775	2080	5.8	0.5	0.5
P15-1	720423	4993795	958.0	2.0	2.2	2.0	0.45	3.95	0.248	60659	3420	14.4	1.1	0.8
P15-2	720423	4993795	948.0	12.0	13.3	2.0	0.45	3.92	0.247	47469	2868	11.4	0.9	0.7
P15-3	720423	4993795	946.0	14.0	15.6	2.0	0.59	5.09	0.247	82263	3501	15.4	1.0	0.7
P16-1*	720720	4994560	1120.0	-	-	2.0	1.00	9.95	0.262	77437	5812	7.5	0.7	0.6
P16-2*	720720	4994570	1120.0	-	-	2.0	1.00	9.95	0.262	126746	4534	12.4	0.8	0.4
P17*	720725	4994175	1121.0	-	-	2.0	0.98	9.76	0.262	176621	6140	17.5	1.1	0.6
P18	720277	4990920	1023.0	-	-	1.5	0.88	8.14	0.254	15718	1698	1.9	0.2	0.2
P19	720256	4990840	1015.0	-	-	1.5	0.96	8.86	0.253	44890	2044	4.9	0.3	0.2
P20	720768	4994151	1117.0	-	-	1.0	0.98	9.86	0.262	123154	4947	12.1	0.8	0.5

^a Location in WGS84 - UTM31N

^b The real depth location of the sample from the top of the scarp

^c The sampling distance from the top of the scarp the natural main slope

^d T is the sample thickness

^e Topographic shielding calculated following Dunne et al. (1999)

^f Results have been corrected from the chemical blank ($^{10}\text{Be}/^9\text{Be}$ blank = $2.46 \pm 0.74 \times 10^{-15}$). Propagated uncertainties include counting statistics, a conservative estimate of 1% for instrumental variability, the uncertainty of the standard deviation and chemical blank.

^g Ages have been computed with the Cronus Calculator (Balco et al., 2008) using the time-dependent scaling scheme of Lal (1991) modified by Stone (2000). Uncertainties are 1σ . Internal uncertainties consider the analytical uncertainties, while the external uncertainties include uncertainty in the production rate (~8%) and uncertainty in the ^{10}Be decay constant (~8%).

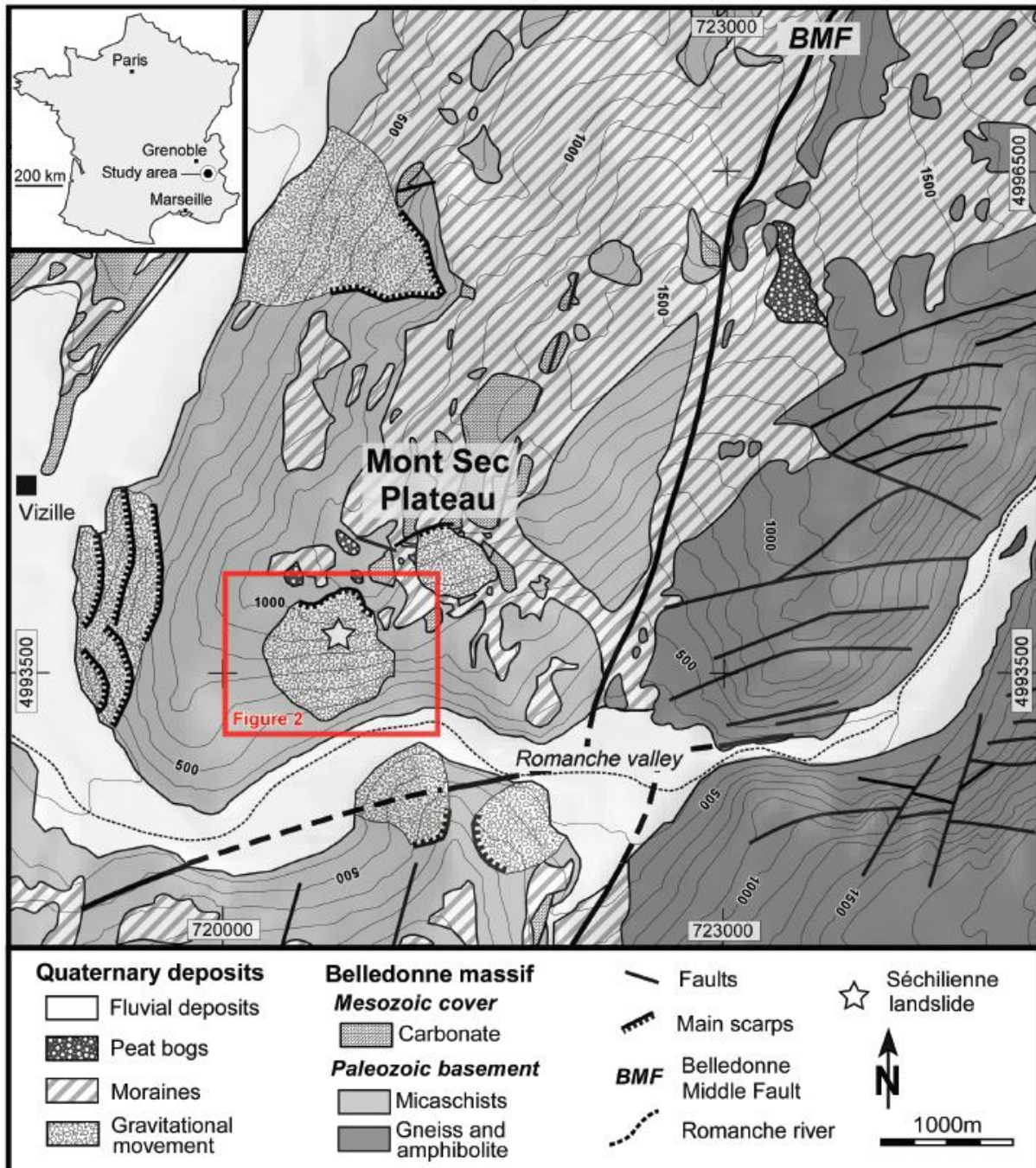


Fig. 1

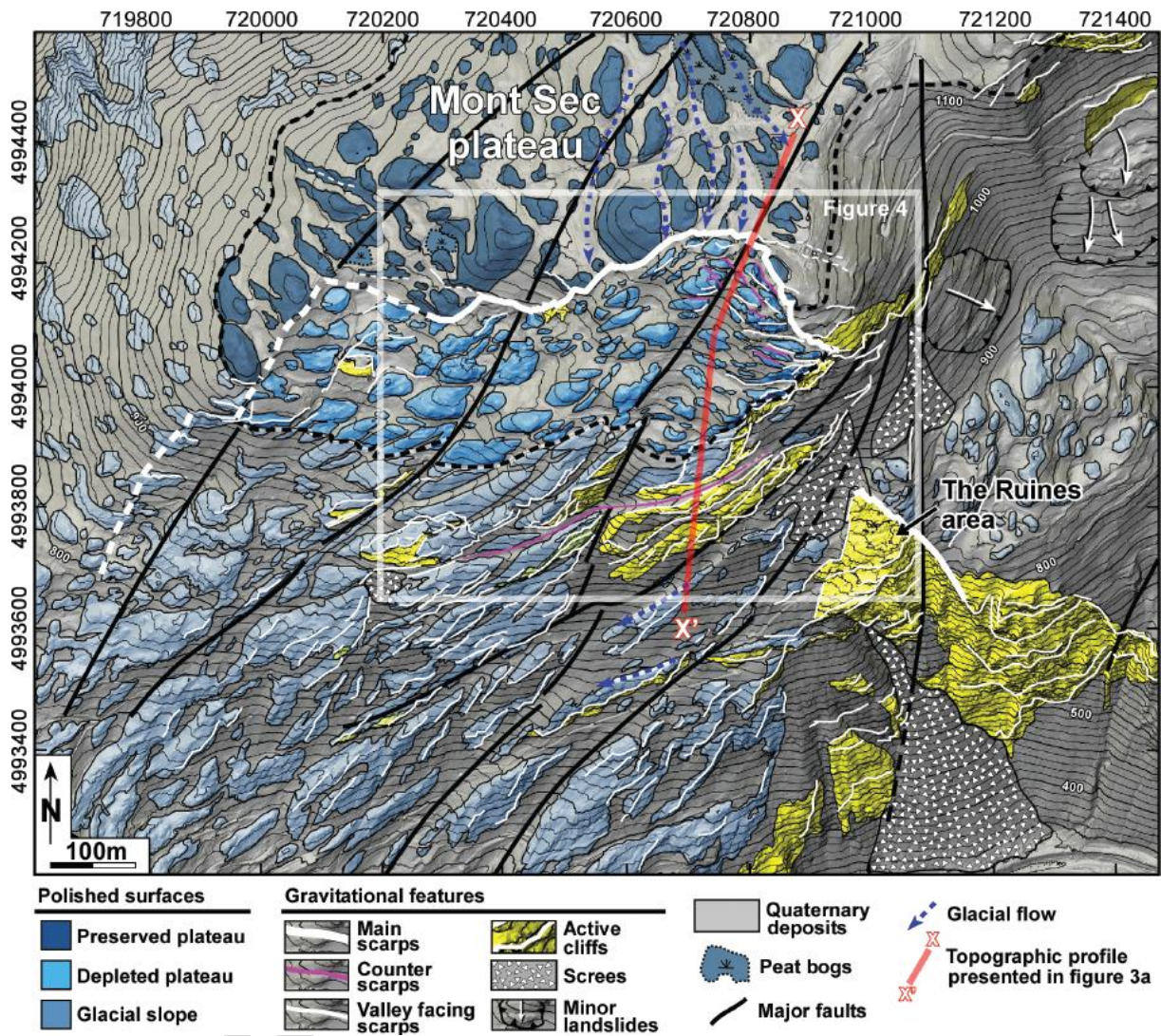


Fig. 2

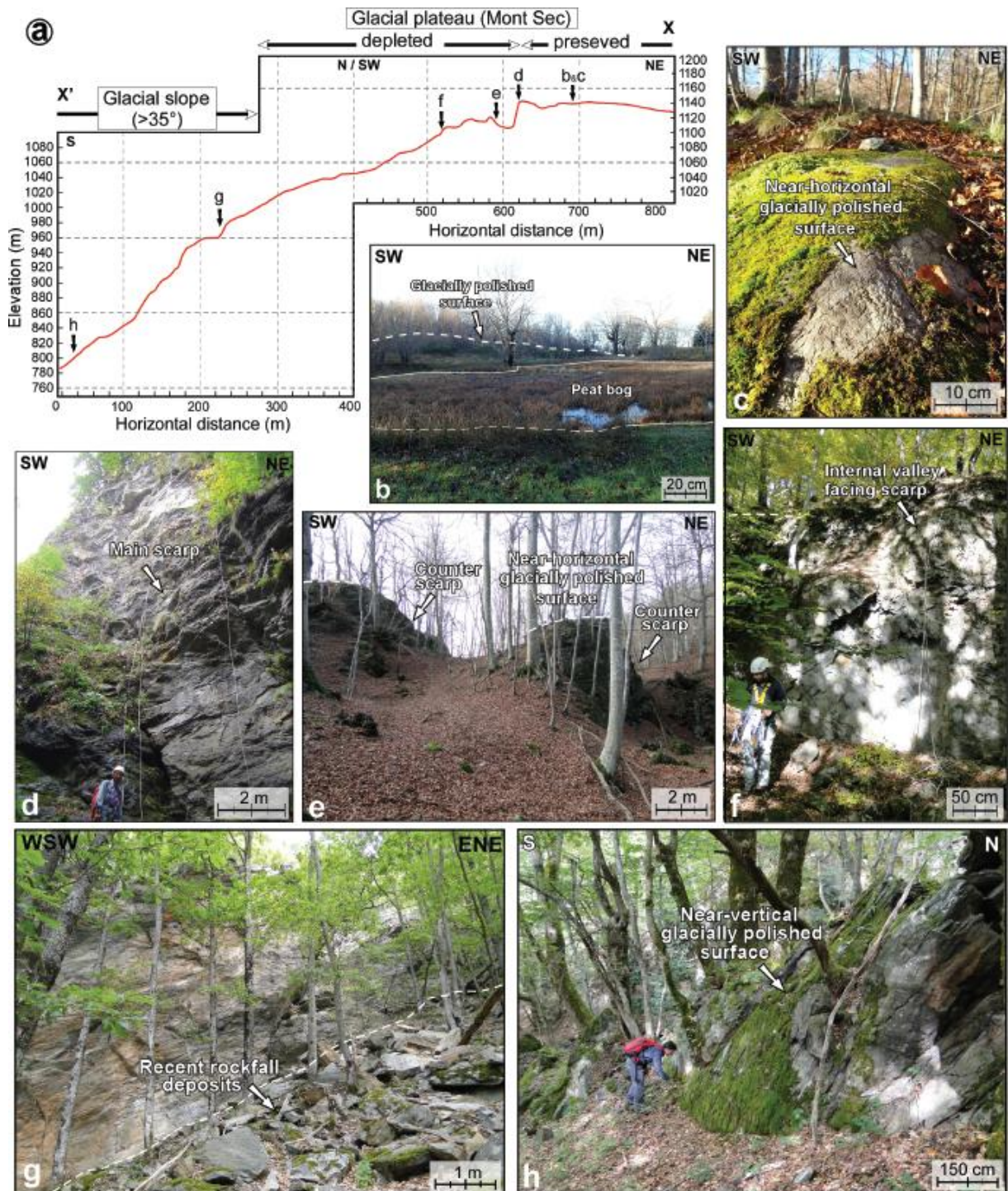


Fig. 3

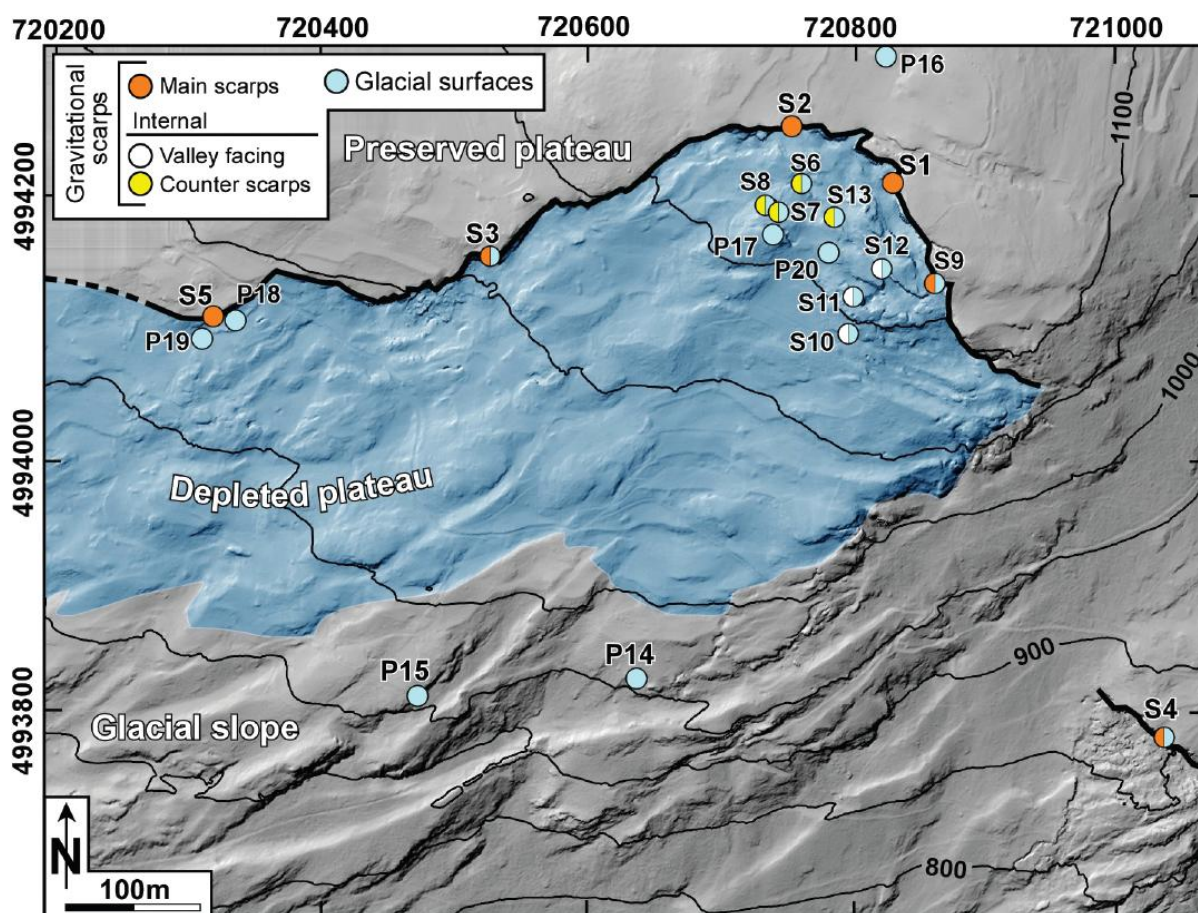


Fig. 4

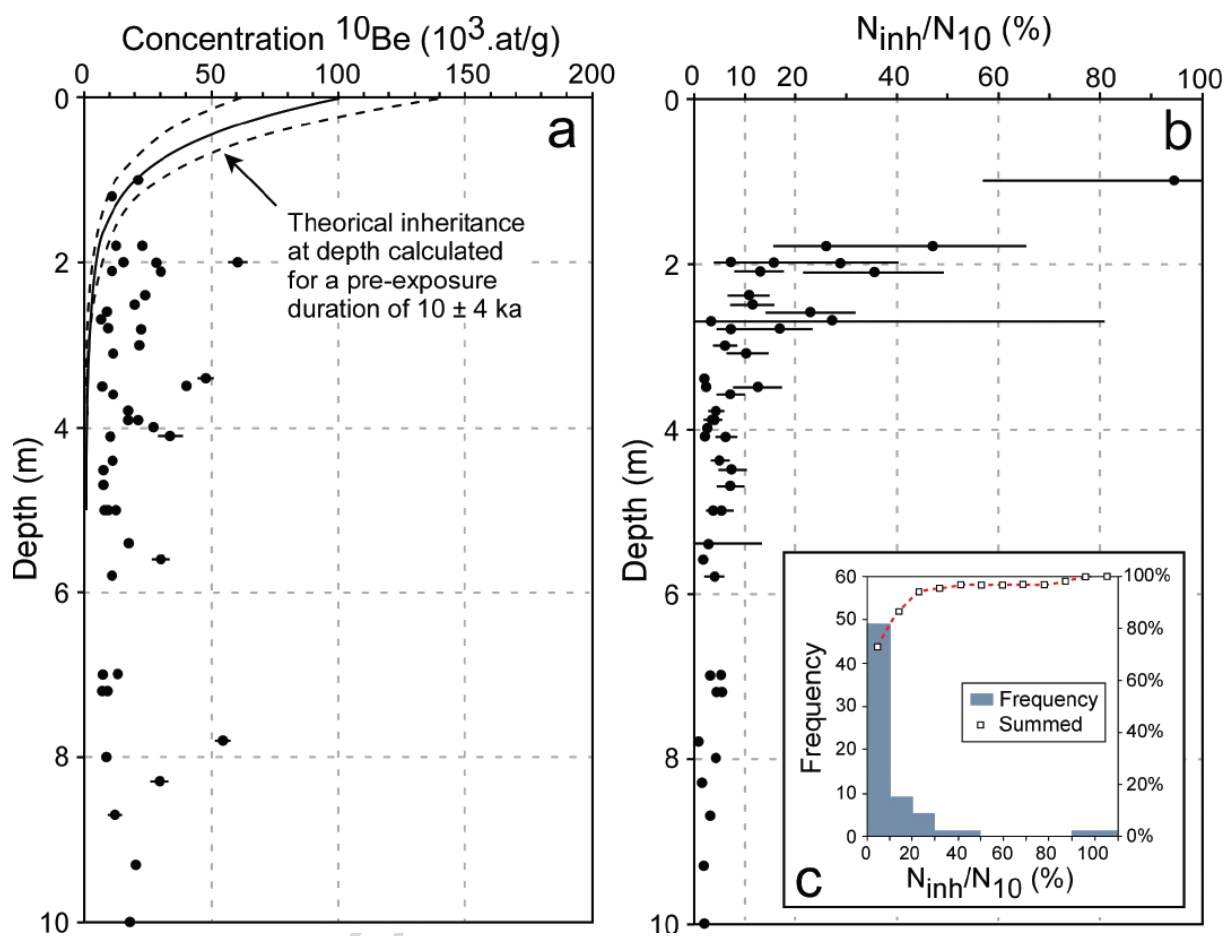


Fig. 5

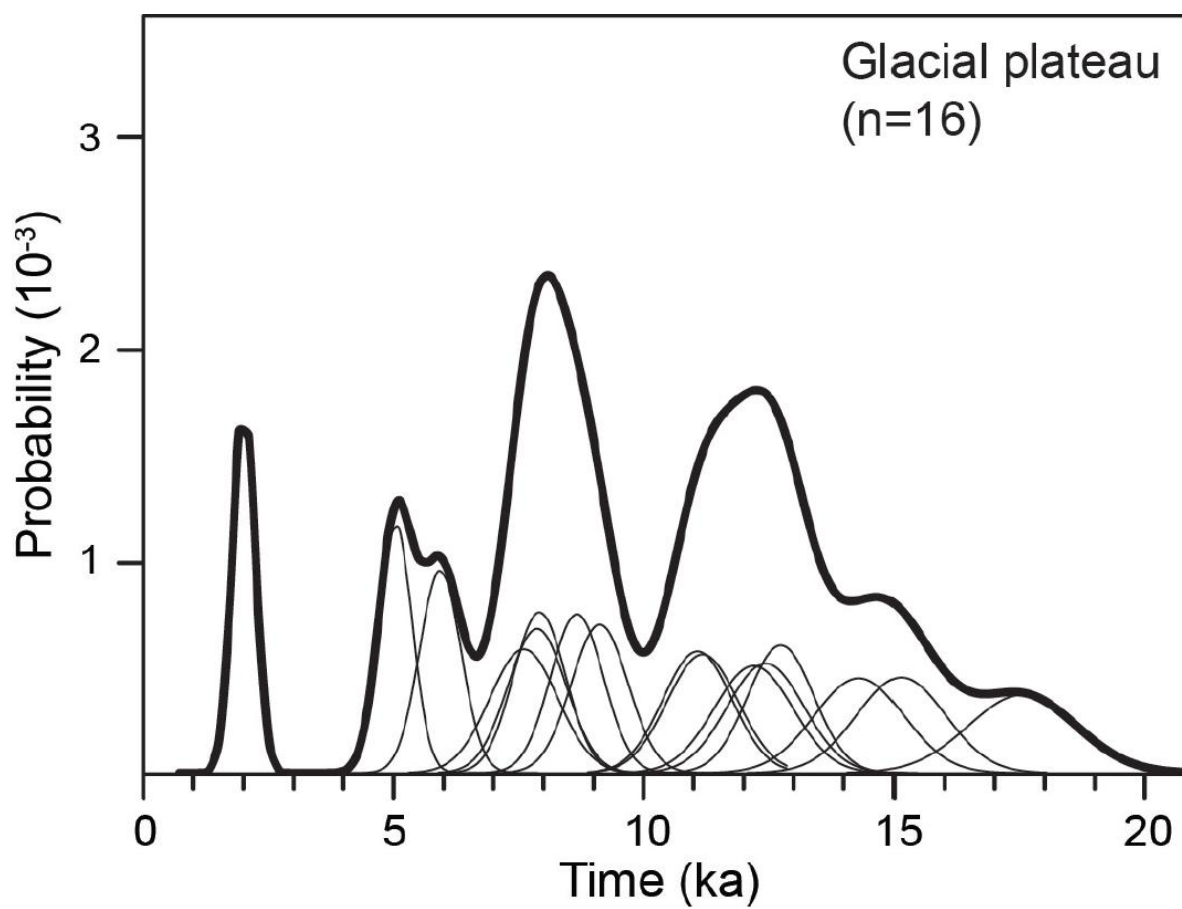


Fig. 6

ACCEPTED

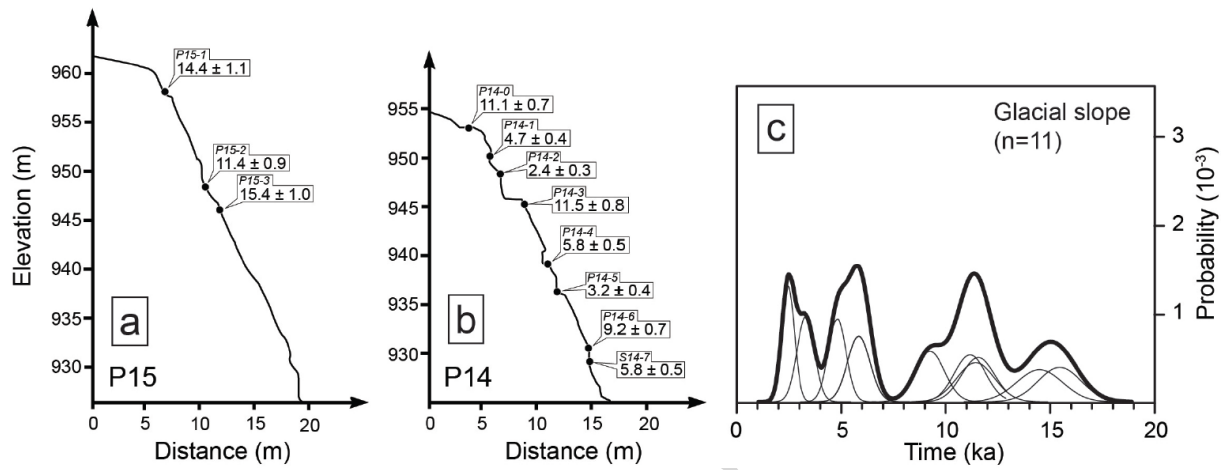


Fig. 7

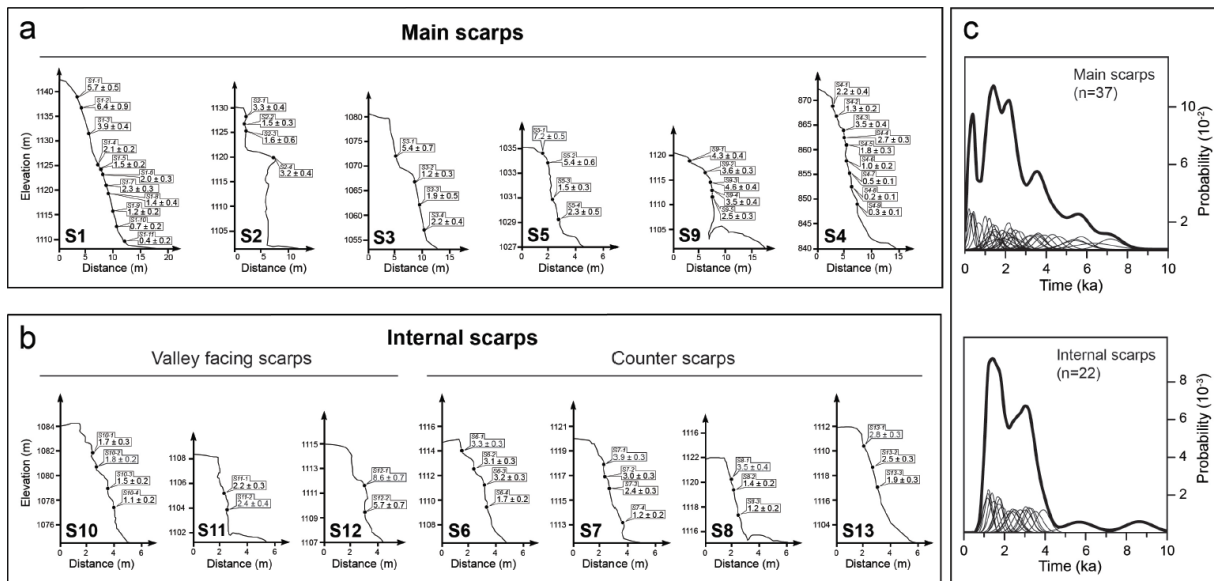


Fig. 8

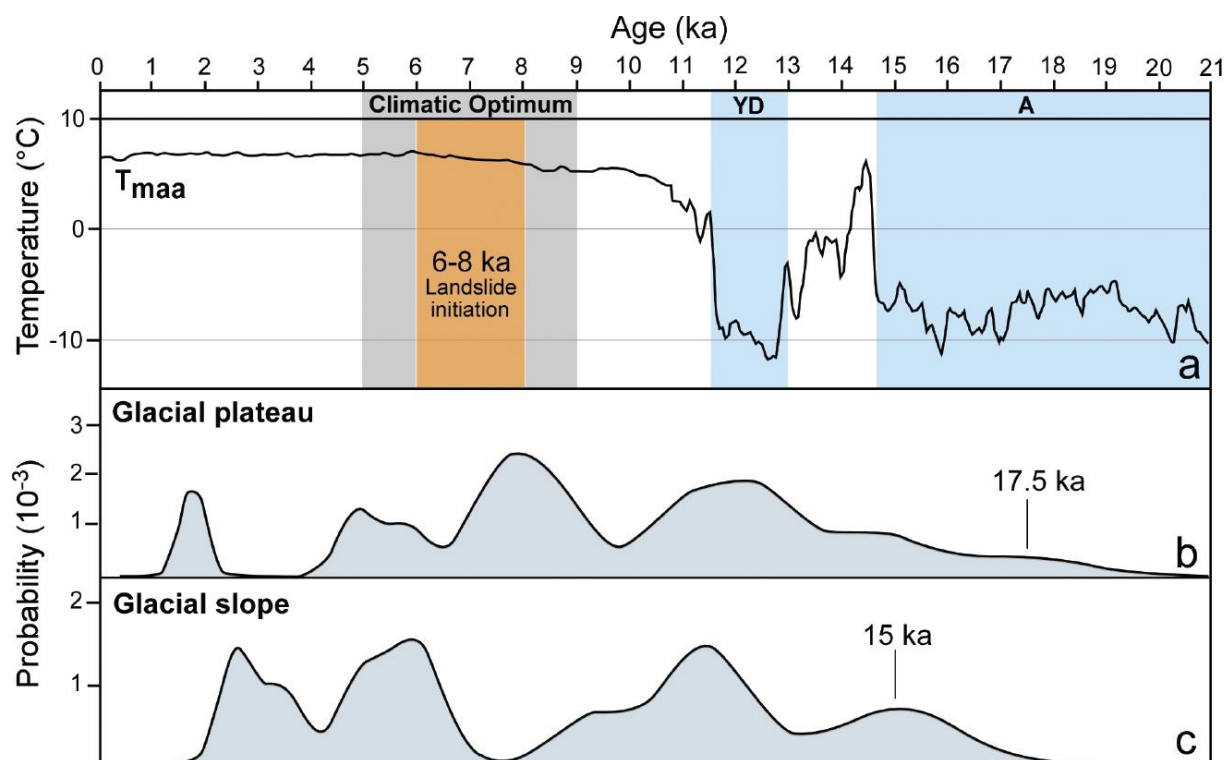


Fig. 9

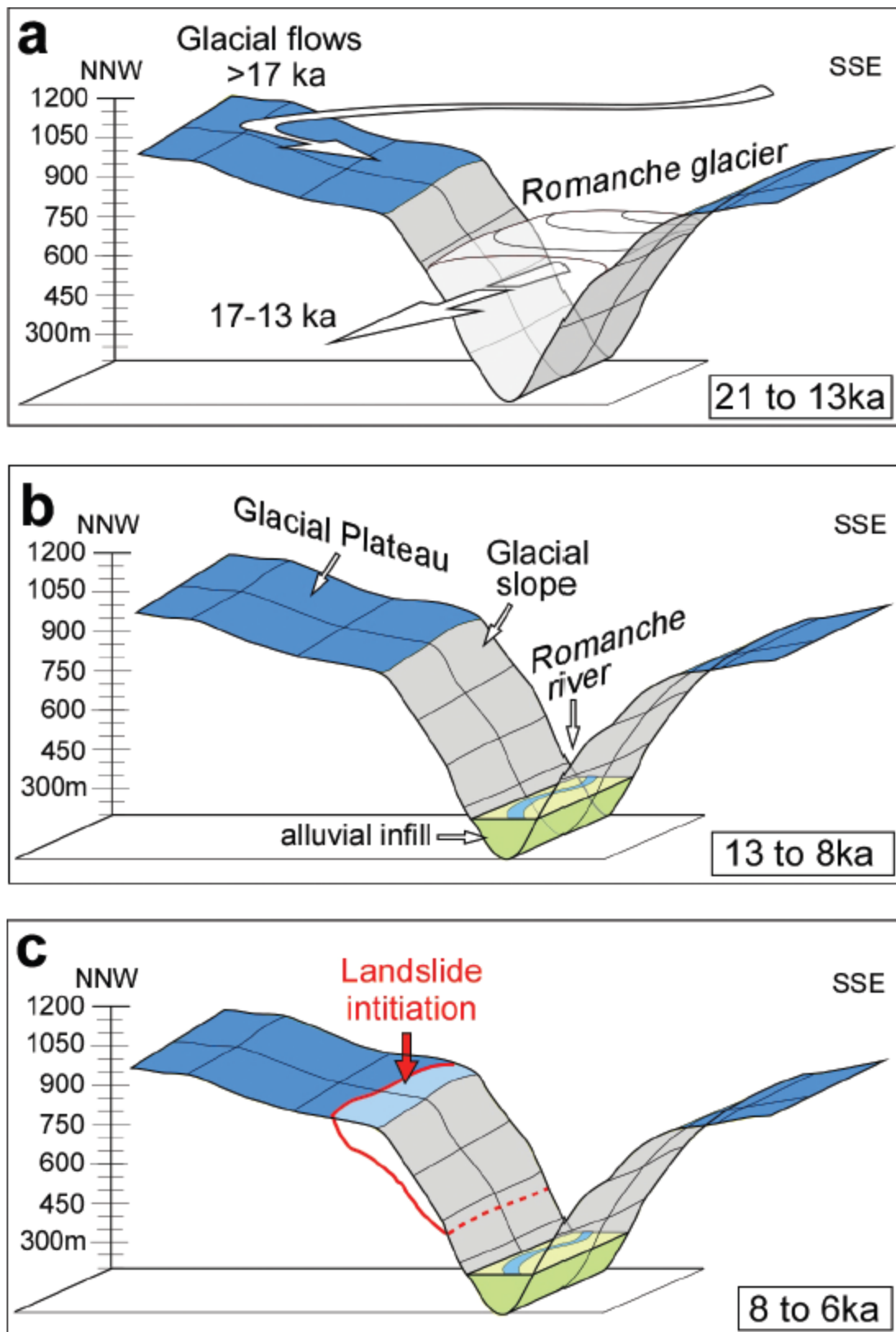


Fig. 10

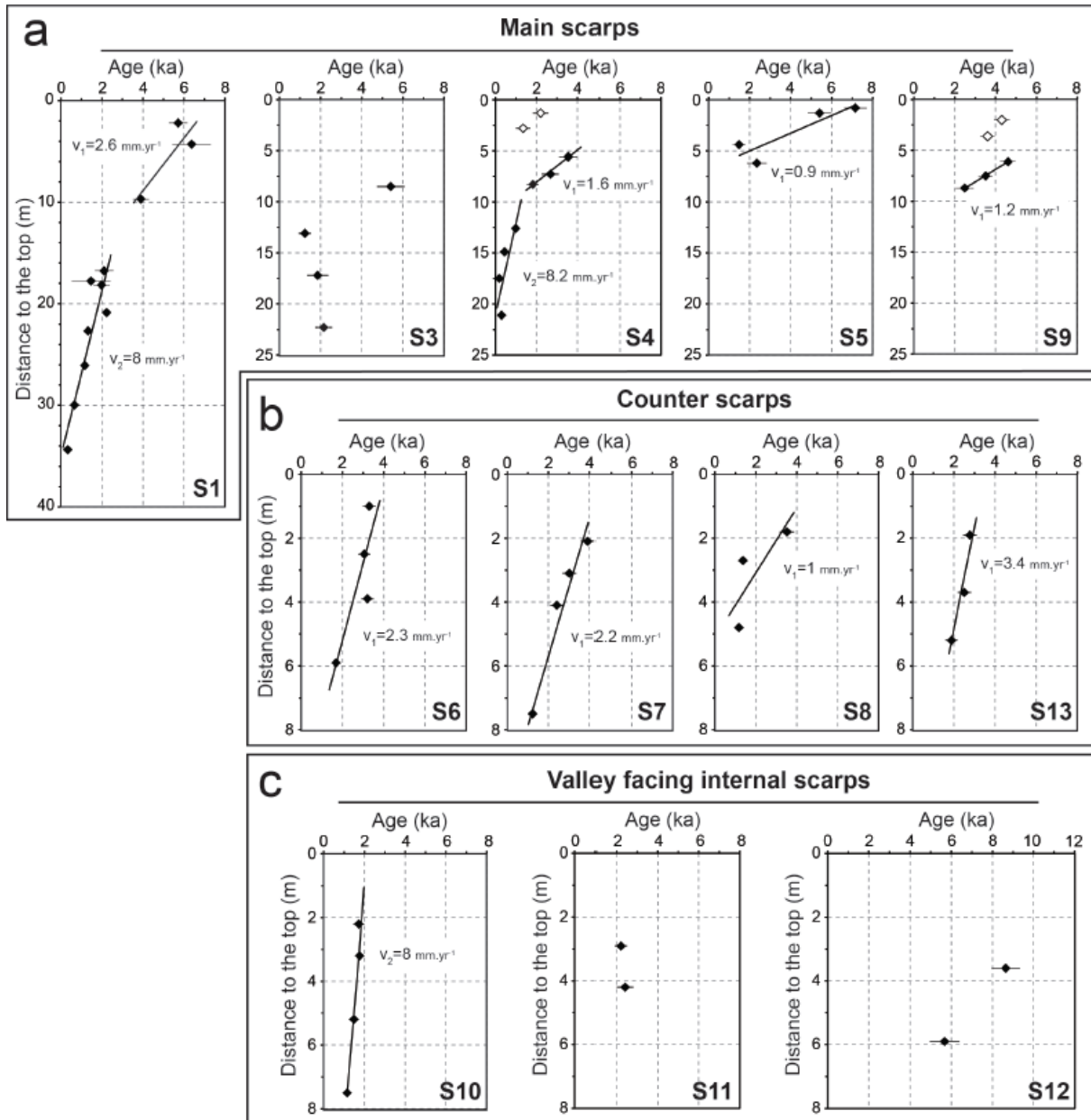


Fig. 11

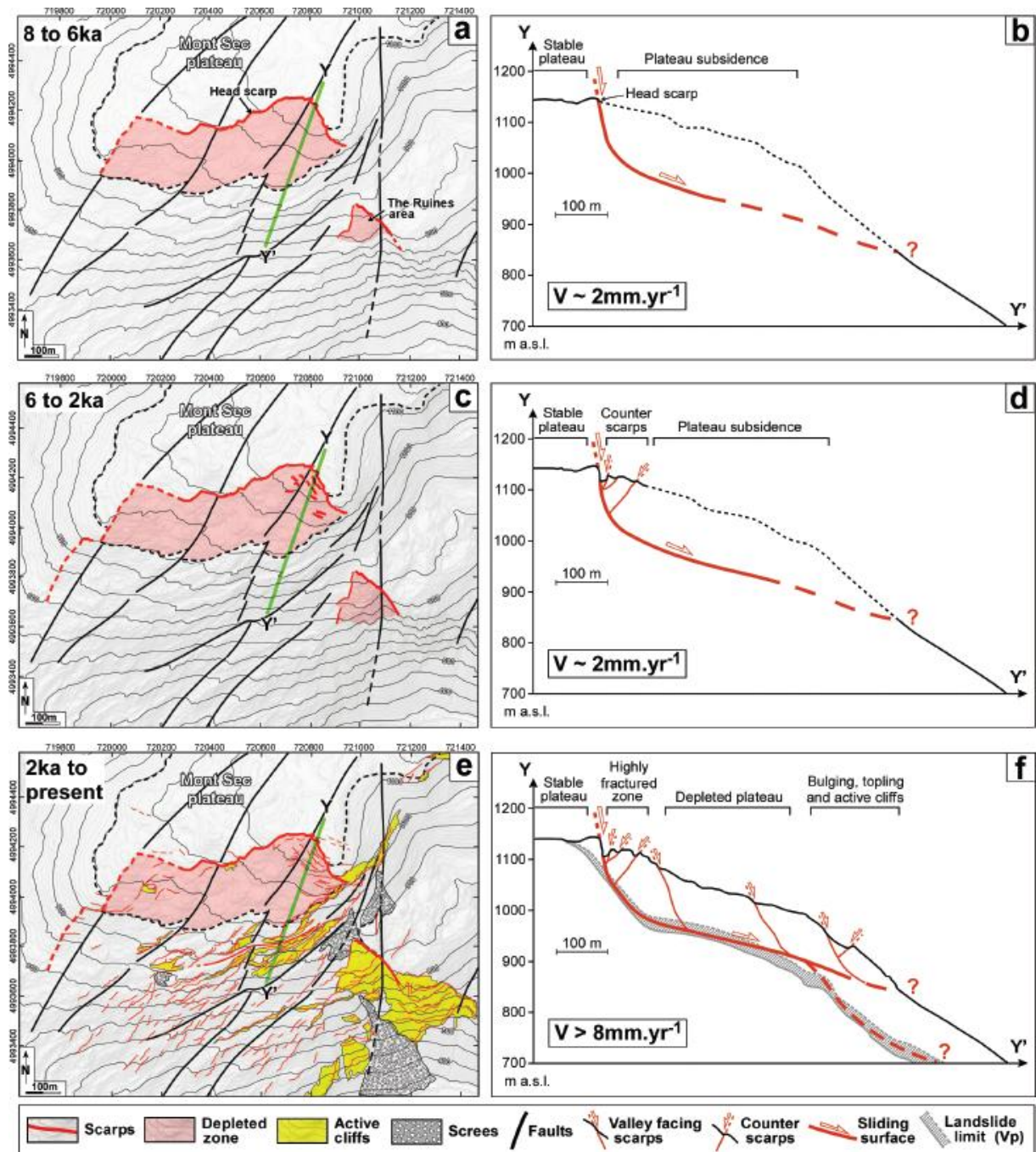


Fig. 12